universität wien

MASTERARBEIT | MASTER'S THESIS

Titel | Title

Spin Dynamics in Hybrid Quantum Systems: Alkali Atoms in Cryogenic Crystals

verfasst von | submitted by

Nikolaos Lagos BSc

angestrebter akademischer Grad | in partial fulfilment of the requirements for the degree of

Master of Science (MSc)

Wien | Vienna, 2025

Studienkennzahl lt. Studienblatt | Degree programme code as it appears on the student record sheet:	UA 066 876
Studienrichtung lt. Studienblatt | Degree programme as it appears on the student record sheet:	Masterstudium Physics
Betreut von | Supervisor:	Univ.-Prof. Dr. Markus Aspelmeyer

Abstract

This thesis presents an experimental investigation of a hybrid quantum system comprising an ensemble of sodium atoms embedded in a neon matrix, strongly coupled to a superconducting microwave resonator operating at millikelvin temperatures. Utilizing principles of cavity quantum electrodynamics, we demonstrate strong collective coupling between the spin ensemble and the resonator, as evidenced by vacuum Rabi splitting in steady-state transmission spectra. The sodium spins are thermally polarized into the lower hyperfine manifold, facilitating coherent interaction with the resonator mode.

Time-domain coherence measurements are performed using Hahn echo and Carr-Purcell-Meiboom-Gill (CPMG) dynamical decoupling sequences. Careful pulse calibration is conducted to optimize the microwave pulse amplitudes and durations for effective spin manipulation. Hahn echo experiments yield a coherence time $T_2 = 768^{+64}_{-53}\,\mu$s at 65 mK, while the CPMG sequence, employing multiple refocusing pulses, extends the coherence time to $T_2 = 1.36^{+0.09}_{-0.06}$ ms, demonstrating suppression of inhomogeneous dephasing and environmental noise. The experimental data are analyzed using fits based on established theoretical models to extract key parameters such as coupling strengths and coherence times.

Spin ensembles in cryogenic quantum solids provide a versatile platform for investigating collective quantum effects in solid-state systems. This thesis offers experimental insights into spin-photon interactions within such hybrid systems and lays groundwork for future research aimed at improving coherence times and exploring potential quantum memory applications.

Kurzfassung

Diese Arbeit präsentiert eine experimentelle Untersuchung eines hybriden Quantensystems, bestehend aus einem Ensemble von Natriumatomen, eingebettet in eine Neonmatrix, das stark mit einem supraleitenden Mikrowellenresonator bei Millikelvin-Temperaturen gekoppelt ist. Unter Anwendung von Prinzipien der Kavitäts-Quantenelektrodynamik demonstrieren wir eine starke kollektive Kopplung zwischen dem Spinensemble und dem Resonator, wie durch Vakuum-Rabi-Splitting in stationären Transmissionsspektren nachgewiesen wird. Die Natriumspins sind thermisch in das niedrigere Hyperfeinniveau polarisiert, was eine kohärente Wechselwirkung mit dem Resonatormodus ermöglicht.

Zeitbereichs-Kohärenzmessungen werden mit Hahn-Echo- und Carr-Purcell-Meiboom-Gill (CPMG)-Sequenzen zur dynamischen Entkopplung durchgeführt. Eine sorgfältige Pulskalibrierung optimiert die Amplituden und Dauern der Mikrowellenpulse für eine effektive Spinmanipulation. Hahn-Echo-Experimente liefern eine Kohärenzzeit von $T_2 = 768^{+64}_{-53}\,\mu$s bei 65 mK, während die CPMG-Sequenz, welche mehrere Refokussierungspulse verwendet, die Kohärenzzeit auf $T_2 = 1.36^{+0.09}_{-0.06}$ ms verlängert und somit eine Unterdrückung inhomogener Dephasierung und Umweltgeräusche demonstriert. Die experimentellen Daten werden durch Anpassungen an etablierte theoretische Modelle analysiert, um Schlüsselparameter wie Kopplungsstärken und Kohärenzzeiten zu extrahieren.

Spinensemble in kryogenen Quantenfestkörpern bieten eine vielseitige Plattform zur Untersuchung kollektiver Quanteneffekte in Festkörpersystemen. Diese Arbeit liefert experimentelle Einblicke in Spin-Photon-Wechselwirkungen in solchen hybriden Systemen und legt die Grundlage für zukünftige Forschungen, die auf die Verbesserung der Kohärenzzeiten und die Erforschung potenzieller Anwendungen als Quanten-Speicher abzielen.

Acknowledgements

I wish to express my sincere gratitude to all who supported me throughout this thesis, contributing significantly to its success.

First, I want to express my deepest gratitude to Andrew and Wenzel. Andrew for his warm and welcoming attitude, continuous support during the experiments, and for generously involving me in his project. Working alongside him was truly motivating and his friendly nature and sense of humor made the lab environment both productive and enjoyable. Being able to explore the system under his guidance was a privilege. Wenzel was the first to introduce me to the group at the Atominstitut and his experiment, serving as an invaluable mentor throughout my early days in the lab. He patiently guided me through the experimental setup, teaching me essential skills ranging from programming and measurement techniques to practical tasks like soldering, cleaning cavities, and other lab work. His deep knowledge provided a solid foundation for my work, and I am grateful for all the things I learned from him.

I am very grateful to Prof. Jörg Schmiedmayer for the opportunity to work in his group at the Atominstitut, and to Lena for her valuable supervision and guidance throughout this work. I also thank Prof. Markus Aspelmeyer from the University of Vienna for supervising this thesis.

Special thanks to Niki, who helped me understand many underlying principles of the experiments. Through numerous in-depth discussions with him, I gained a much clearer understanding of why things work the way they do, which greatly enriched my learning experience.

Lastly, I want to express my deepest gratitude to my family, including my father, mother, and sister, for their support along this journey. To my partner, thank you for your endless love, patience, and understanding. Your belief in me has been a constant source of comfort and motivation, especially during the toughest moments. I am also truly grateful to my friends, whose encouragement has meant so much along the way.

Contents

1 Introduction

The study of light-matter interaction has long been a central focus of physics, leading to profound discoveries that have shaped modern science. Maxwell's equations laid the foundation for understanding electrodynamics, unifying the concepts of electricity, magnetism, and optics [1]. These equations, however, could not explain phenomena such as the photoelectric effect, where light ejects electrons from a material's surface. This was resolved by Einstein, who proposed that light is quantized into discrete packets of energy called photons [2]. This revolutionary idea not only earned him the Nobel Prize [3] but also paved the way for the development of quantum mechanics, a profound shift in our understanding of the microscopic world. Building on this foundation, the quantization of the electromagnetic field gave rise to quantum electrodynamics (QED), a theory that describes how light and matter interact at the quantum level and has become a cornerstone of modern physics [4].

Building on these theoretical advancements, cavity quantum electrodynamics (cavity QED) emerged as a field dedicated to studying the interaction of quantized electromagnetic fields with matter confined in optical or microwave cavities [5]. These systems have enabled precise control over individual quantum emitters such as atoms, ions, quantum dots, and superconducting qubits. By confining electromagnetic fields within a cavity, the light-matter interaction is enhanced [6], making cavity QED an invaluable platform for exploring fundamental quantum phenomena. Over the past few decades, this approach has also enabled practical applications in quantum information processing, quantum sensing, and the development of hybrid quantum systems [7]. Cavity QED systems have long explored the coupling of spin ensembles to resonators, where the collective enhancement of the coupling strength allowed early access to the strong coupling regime [8], well before this became feasible with individual spins. In recent years, interest in these ensemble-based systems has resurged, particularly within hybrid quantum architectures that combine different quantum components to leverage their complementary strengths. Such systems have been used to study a range of collective quantum effects [9], including superradiance [10, 11], spin coherence protection [12], and non-Markovian dynamics [13].

This thesis focuses on a hybrid quantum system comprising a large ensemble of sodium spins embedded in a neon matrix coupled to a superconducting resonator.

This system operates at cryogenic temperatures, allowing long spin coherence times and enabling us to achieve strong collective coupling between the spin ensemble and the resonator. In this platform, several system parameters can be adjusted, including the spin density of the ensemble, the type of atomic impurity, and the choice of cryogenic host matrix. This flexibility, together with the long coherence times at millikelvin temperatures, makes the system well-suited for studying collective spin-photon interactions and coherence effects.

The structure of this thesis is as follows. Chapter 2 presents the theoretical framework underlying the experiment, including a detailed discussion of cavity QED and the Tavis-Cummings model, which describes the interaction between a spin ensemble and a cavity. Chapter 3 describes the experimental setup, highlighting the design and operation of the superconducting resonator, the Adiabatic Demagnetization Refrigerator (ADR), and the microwave setup used for signal generation and detection. Chapter 4 presents the experimental results, where we investigate the coherence properties of the sodium spin ensemble and demonstrate strong coupling effects, such as vacuum Rabi splitting and collective dynamics, followed by a discussion of the experimental results in Chapter 5, as well as an outline for potential directions for future research.

By studying this hybrid quantum system, we aim to contribute to the understanding of collective quantum phenomena in spin ensembles, paving the way for advancements in quantum technologies and the exploration of fundamental physics.

2 Theoretical Background

2.1 Cavity Quantum Electrodynamics

Cavity quantum electrodynamics studies the interaction between quantized light and matter within a cavity. The cavity, which supports a quantized mode of the electromagnetic field, is illustrated in figure 2.1. In order to be able to describe such an interaction, we begin by quantizing the electromagnetic field. Next, we introduce the Jaynes-Cummings model, a theoretical framework which models the interaction of a two-level system, such as a two-level atom or a spin, with a single mode of the quantized field, leading to phenomena like Rabi oscillations. The chapter concludes with the Tavis-Cummings Hamiltonian, a model which extends the Jaynes-Cummings model to multiple spin systems. These theoretical models are particularly relevant as a foundation for understanding our experimental system, which consists of a spin ensemble coupled to a superconducting microwave cavity and will be described in detail in Chapter 3. For this section, several books [14–16] have been used as sources for the various derivations and formulas.

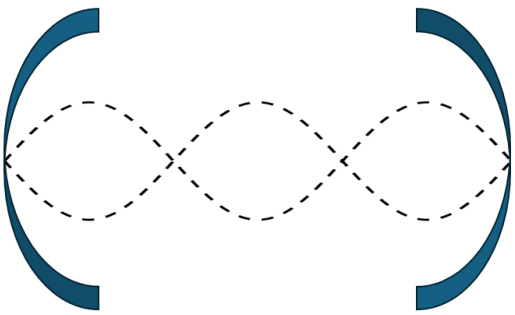

Figure 2.1: Schematic of a single-mode cavity formed by two mirrors, depicting the spatial standing wave of the cavity mode, which will be quantized in the following section 2.1.1.

2.1.1 Quantization of the Electromagnetic Field

We assume a quantized description of the electromagnetic field, where the cavity mode is treated as a quantum harmonic oscillator. A full derivation of this formalism can be found in standard quantum optics literature, such as [16]. In order to quantize the electromagnetic field we begin by looking at the classical description of the field based on the Maxwell's equations. In free space, assuming no charges or currents, the Maxwell's equations take the form:

$$\begin{aligned} \vec{\nabla} \cdot \vec{\mathbf{E}} &= 0 \\ \vec{\nabla} \cdot \vec{\mathbf{B}} &= 0 \\ \vec{\nabla} \times \vec{\mathbf{E}} &= -\frac{\partial \vec{\mathbf{B}}}{\partial t} \\ \vec{\nabla} \times \vec{\mathbf{B}} &= \epsilon_0 \mu_0 \frac{\partial \vec{\mathbf{E}}}{\partial t} \end{aligned} \tag{2.1}$$

where ϵ_0 is the permittivity and μ_0 is the permeability of free space. It is useful to introduce a vector potential $\vec{\mathbf{A}}$ such that

$$\vec{\mathbf{B}} = \vec{\nabla} \times \vec{\mathbf{A}} \tag{2.2}$$

which, by construction, satisfies the equation for the divergence of the magnetic field:

$$\vec{\nabla} \cdot \vec{\mathbf{B}} = \vec{\nabla} \cdot (\vec{\nabla} \times \vec{\mathbf{A}}) = 0$$

The electric field in this case takes the form

$$\begin{aligned} \vec{\nabla} \times \vec{\mathbf{E}} &= -\frac{\partial (\vec{\nabla} \times \vec{\mathbf{A}})}{\partial t} = -\vec{\nabla} \times \frac{\partial \vec{\mathbf{A}}}{\partial t} \\ \rightarrow \vec{\mathbf{E}} &= -\vec{\nabla}\phi - \frac{\partial \vec{\mathbf{A}}}{\partial t} \end{aligned} \tag{2.3}$$

where ϕ is a scalar field. The scalar and vector potentials used to describe the electric and magnetic fields are not unique in the sense that different choices of ϕ and $\vec{\mathbf{A}}$ can result in the same electromagnetic fields $\vec{\mathbf{E}}$ and $\vec{\mathbf{B}}$ which is known as gauge freedom. Specifically, using the gauge transformation with a scalar function $\mathbf{\Lambda}(\tilde{\mathbf{r}}, \mathbf{t})$, we obtain:

$$\begin{aligned} \phi &\to \phi - \frac{\partial \mathbf{\Lambda}}{\partial t} \\ \vec{\mathbf{A}} &\to \vec{\mathbf{A}} + \vec{\nabla}\mathbf{\Lambda} \end{aligned} \tag{2.4}$$

and the fields $\vec{\mathbf{E}}$ and $\vec{\mathbf{B}}$ in equations (2.2) and (2.3) are left unchanged. A commonly used gauge is the Coulomb gauge:

$$\vec{\nabla} \cdot \vec{\mathbf{A}} = 0 \tag{2.5}$$

By inserting the expressions (2.2) and (2.3) into the Maxwell's equation for the rotation of the $\vec{\mathbf{B}}$ field (2.1) we get

$$\vec{\nabla} \times (\vec{\nabla} \times \vec{\mathbf{A}}) = -\epsilon_0 \mu_0 \frac{\partial}{\partial t} \left(\vec{\nabla}\phi + \frac{\partial \vec{\mathbf{A}}}{\partial t} \right) .$$

By using the identity

$$\vec{\nabla} \times (\vec{\nabla} \times \vec{\mathbf{A}}) = \vec{\nabla}(\vec{\nabla} \cdot \vec{\mathbf{A}}) - \vec{\nabla}^2 \vec{\mathbf{A}}$$

and the Coulomb gauge (2.5) and assuming no sources ($\phi = 0$) we arrive at:

$$\vec{\nabla}^2 \vec{\mathbf{A}} - \epsilon_0 \mu_0 \frac{\partial^2 \vec{\mathbf{A}}}{\partial t^2} = 0 \tag{2.6}$$

which is a wave equation for the vector potential $\vec{\mathbf{A}}$ with the velocity

$$c = \frac{1}{\sqrt{\epsilon_0 \mu_0}}$$

The general plane wave solution can be expressed as

$$\vec{\mathbf{A}}(\vec{r}, t) = \vec{\mathbf{A}_0} \cdot e^{i(\vec{k} \cdot \vec{r} - \omega t)} \tag{2.7}$$

with the dispersion relation

$$k = \frac{\omega}{c}$$

Here, ω is the angular frequency of the mode, $\vec{k}$ is the wavevector, and c is the speed of light in vacuum. We now consider a cubic cavity of side length L with perfectly reflecting walls to model the quantized modes of the electromagnetic field. For a perfectly conducting cavity, the tangential component of the electric field must vanish at the boundaries, leading to the formation of standing wave modes:

$$e^{ik_x x} = e^{ik_x(x+L)}$$

from which we get

$$k_x = \left(\frac{2\pi}{L}\right) n_x, \quad n_x \in \mathbb{Z}$$

The wave vector $\vec{k}$ for all three directions is then

$$\vec{k} = \frac{2\pi}{L}(n_x, n_y, n_z) \tag{2.8}$$

We can now express the vector potential as a superposition of the form

$$\vec{\mathbf{A}}(\vec{r}, t) = \sum_k \sum_{\lambda=\pm 1} \vec{\epsilon_\lambda} \left(A_{k\lambda} \cdot e^{i(\vec{k}\cdot\vec{r} - \omega_k t)} + A^*_{k\lambda} \cdot e^{-i(\vec{k}\cdot\vec{r} - \omega_k t)} \right) \tag{2.9}$$

where $A_{k\lambda}$ is the complex amplitude of the field $\vec{\mathbf{A}}$ and $\vec{\epsilon_\lambda}$ the real polarisation vector over the two orthogonal polarisations. Any mode in the cube is specified by the vector $\vec{k}$, i.e. the set of integers (n_x, n_y, n_z) (2.8). Using equations (2.2) and (2.3) we get the expressions for the $\vec{\mathbf{E}}$ and $\vec{\mathbf{B}}$ fields:

$$\vec{\mathbf{E}}(\vec{r}, t) = i \sum_k \sum_{\lambda=\pm 1} \omega_k \vec{\epsilon_\lambda} \left(A_{k\lambda} \cdot e^{i(\vec{k}\cdot\vec{r} - \omega_k t)} - A^*_{k\lambda} \cdot e^{-i(\vec{k}\cdot\vec{r} - \omega_k t)} \right) \tag{2.10}$$

$$\vec{\mathbf{B}}(\vec{r}, t) = i \sum_k \sum_{\lambda=\pm 1} \left(\vec{k} \times \vec{\epsilon_\lambda} \right) \left(A_{k\lambda} \cdot e^{i(\vec{k}\cdot\vec{r} - \omega_k t)} - A^*_{k\lambda} \cdot e^{-i(\vec{k}\cdot\vec{r} - \omega_k t)} \right) \tag{2.11}$$

The energy of the field is given by:

$$H = \frac{1}{2} \int_V \left(\epsilon_0 \vec{\mathbf{E}}^2 + \frac{1}{\mu_0} \vec{\mathbf{B}}^2 \right) d^3V$$

Using equations (2.10) and (2.11) for the electromagnetic fields we arrive at the following:

$$H = 2\epsilon_0 V \sum_k \sum_{\lambda=\pm 1} \omega_k^2 A_{k\lambda} A^*_{k\lambda} \tag{2.12}$$

By introducing canonical variables $q_{k\lambda}$ and $p_{k\lambda}$ such that

$$A_{k\lambda} = \frac{1}{2\omega_k \sqrt{\epsilon_0 V}} \left(\omega_k q_{k\lambda} + i p_{k\lambda} \right) \tag{2.13}$$

$$A^*_{k\lambda} = \frac{1}{2\omega_k \sqrt{\epsilon_0 V}} \left(\omega_k q_{k\lambda} - i p_{k\lambda} \right) \tag{2.14}$$

we can rewrite the field energy as

$$H = \frac{1}{2}\sum_{k}\sum_{\lambda=\pm1}\left(p_{k\lambda}^2 + \omega_k^2 q_{k\lambda}^2\right) \tag{2.15}$$

In order to quantize the electromagnetic field we interpret the canonical variables as operators which satisfy the following commutation relations

$$\begin{aligned}[\hat{q}_{k\lambda}, \hat{q}_{k'\lambda'}] &= [\hat{p}_{k\lambda}, \hat{p}_{k'\lambda'}] = 0 \\ [\hat{q}_{k\lambda}, \hat{p}_{k'\lambda'}] &= i\hbar\delta_{kk'}\delta_{\lambda\lambda'}\end{aligned} \tag{2.16}$$

where the field amplitudes now take the form of the annihilation and creation operators defined as

$$\hat{a}_{k\lambda} = \frac{1}{\sqrt{2\hbar\omega_k}}\left(\omega_k\hat{q}_{k\lambda} + i\hat{p}_{k\lambda}\right) \tag{2.17}$$

$$\hat{a}_{k\lambda}^\dagger = \frac{1}{\sqrt{2\hbar\omega_k}}\left(\omega_k\hat{q}_{k\lambda} - i\hat{p}_{k\lambda}\right) \tag{2.18}$$

which satisfy the bosonic commutation relations:

$$\begin{aligned}[\hat{a}_{k\lambda}, \hat{a}_{k'\lambda'}] &= [\hat{a}_{k\lambda}^\dagger, \hat{a}_{k'\lambda'}^\dagger] = 0 \\ [\hat{a}_{k\lambda}, \hat{a}_{k'\lambda'}^\dagger] &= \delta_{kk'}\delta_{\lambda\lambda'}\end{aligned} \tag{2.19}$$

The field energy (2.15) written with respect to the annihilation and creation operators takes the form of the Hamiltonian operator

$$\hat{H} = \sum_{k}\sum_{\lambda=\pm1}\hbar\omega_k\left(\hat{a}_{k\lambda}^\dagger\hat{a}_{k\lambda} + \frac{1}{2}\right) \tag{2.20}$$

The quantized forms of the vector potential $\vec{\mathbf{A}}(\vec{r},t)$ and the fields $\vec{\mathbf{E}}(\vec{r},t)$ and $\vec{\mathbf{B}}(\vec{r},t)$ are

$$\begin{aligned}\hat{\mathbf{A}}(\vec{r},t) &= \sum_{k}\sum_{\lambda=\pm1}\sqrt{\frac{\hbar}{2\omega_k\epsilon_0 V}}\vec{\epsilon_\lambda}\left(\hat{a}_{k\lambda}\cdot e^{i(\vec{k}\cdot\vec{r}-\omega_k t)} + \hat{a}_{k\lambda}^\dagger\cdot e^{-i(\vec{k}\cdot\vec{r}-\omega_k t)}\right) \\ \hat{\mathbf{E}}(\vec{r},t) &= i\sum_{k}\sum_{\lambda=\pm1}\sqrt{\frac{\hbar\omega_k}{2\epsilon_0 V}}\vec{\epsilon_\lambda}\left(\hat{a}_{k\lambda}\cdot e^{i(\vec{k}\cdot\vec{r}-\omega_k t)} - \hat{a}_{k\lambda}^\dagger\cdot e^{-i(\vec{k}\cdot\vec{r}-\omega_k t)}\right)\end{aligned} \tag{2.21}$$

$$\hat{\mathbf{B}}(\vec{r},t) = i\sum_{k}\sum_{\lambda=\pm1}\sqrt{\frac{\hbar}{2\omega_k\epsilon_0 V}}\left(\vec{k}\times\vec{\epsilon_\lambda}\right)\left(\hat{a}_{k\lambda}\cdot e^{i(\vec{k}\cdot\vec{r}-\omega_k t)} - \hat{a}^\dagger_{k\lambda}\cdot e^{-i(\vec{k}\cdot\vec{r}-\omega_k t)}\right)$$

2.1.2 Jaynes-Cummings Hamiltonian

Now that we have quantized the electromagnetic field, we can study its interaction with matter. In general, atoms and other quantum emitters possess multiple internal energy levels, but for many scenarios, especially near-resonant interactions, it is sufficient to approximate the system as a two-level emitter. The Jaynes-Cummings model provides a theoretical framework for describing the interaction between such a two-level system and a single mode of the quantized electromagnetic field within a cavity. To derive the Jaynes-Cummings Hamiltonian, we begin by considering the Hamiltonian of a two-level atom in the presence of an electromagnetic field [17]:

$$\hat{H}(\vec{r},t) = \frac{1}{2m}[\hat{p} + e\vec{\mathbf{A}}(\vec{r},t)]^2 + V(\vec{r}) \tag{2.22}$$

with $\vec{\mathbf{A}}$ as the vector potential in the Coulomb gauge ($\nabla\cdot\vec{\mathbf{A}} = 0$),

The time-dependent Schrödinger equation has the form

$$i\hbar\frac{\partial\psi(\vec{r},t)}{\partial t} = \hat{H}(\vec{r},t)\psi(\vec{r},t) \tag{2.23}$$

In order to simplify the calculation we define a unitary operator $\hat{U}$ such that

$$\psi(\vec{r},t) = \hat{U}\phi(\vec{r},t) \tag{2.24}$$

Taking the time derivative gives us

$$\frac{\partial}{\partial t}\psi(\vec{r},t) = \frac{\partial\hat{U}}{\partial t}\phi(\vec{r},t) + \hat{U}\frac{\partial}{\partial t}\phi(\vec{r},t) \tag{2.25}$$

Plugging this into the Schrödinger equation (2.23) yields

$$i\hbar\frac{\partial\hat{U}}{\partial t}\phi(\vec{r},t) + i\hbar\hat{U}\frac{\partial}{\partial t}\phi(\vec{r},t) = \hat{H}(\vec{r},t)\hat{U}\phi(\vec{r},t)$$

Multiplying both sides of the equation with $\hat{U}^\dagger$ gives us

$$i\hbar\frac{\partial}{\partial t}\phi(\vec{r},t) = \hat{H}'(\vec{r},t)\phi(\vec{r},t) \tag{2.26}$$

with

$$\hat{H}'(\vec{r},t) = \hat{U}^\dagger \hat{H}(\vec{r},t)\hat{U} - i\hbar\hat{U}^\dagger \frac{\partial \hat{U}}{\partial t} \tag{2.27}$$

We now consider a general unitary transformation of the form:

$$\hat{U} = e^{i\chi(\vec{r},t)} \tag{2.28}$$

where $\chi(\vec{r},t)$ is a scalar function with spatial and temporal dependencies. We now explore how the Hamiltonian (2.27) transforms in this case

$$\begin{aligned} \hat{H}'(\vec{r},t) = \hat{U}^\dagger \hat{H}(\vec{r},t)\hat{U} - i\hbar\hat{U}^\dagger \frac{\partial \hat{U}}{\partial t} = \\ = \frac{1}{2m}[\hat{p} + \hbar\vec{\nabla}\chi(\vec{r},t) + e\vec{\mathbf{A}}(\vec{r},t)]^2 + V(\vec{r}) + \hbar\frac{\partial \chi(\vec{r},t)}{\partial t} \end{aligned} \tag{2.29}$$

The derivation of this result is shown in Appendix A.1.

For $|\vec{r}|$ of typical atomic dimensions (a few Angstroms) and λ of typical optical or microwave wavelengths it is true that $\vec{k}\cdot\vec{r} \ll 1$ so that over the extent of an atom, the vector potential is spatially uniform: $\vec{A}(\vec{r},t) \approx \vec{A}(t)$. This is the so-called dipole approximation [14]. We now use the gauge function $\chi(\vec{r},t) = -\frac{e}{\hbar}\cdot\vec{A}(t)\cdot\vec{r}$ with

$$\vec{\nabla}\chi(\vec{r},t) = -\frac{e}{\hbar}\cdot\vec{A}(t) \tag{2.30}$$

$$\frac{\partial}{\partial t}\chi(\vec{r},t) = -\frac{e}{\hbar}\cdot\vec{r}\cdot\frac{\partial}{\partial t}\vec{A}(t) = \frac{e}{\hbar}\cdot\vec{r}\cdot\vec{E}(t) \tag{2.31}$$

Thus the Hamiltonian takes the form

$$\begin{aligned} \hat{H}'(\vec{\mathbf{r}},t) = \frac{\hat{p}^2}{2m} + V(\vec{r}) + e\vec{\mathbf{r}}\cdot\vec{E}(t) \\ \rightarrow \hat{H}'(\vec{r},t) = \hat{H}_0(\vec{r},t) - \vec{d}\cdot\vec{E}(t) \end{aligned} \tag{2.32}$$

with $\vec{d} = -e\cdot\vec{r}$ as the dipole moment.

Now that we have derived the form of the Hamiltonian in the dipole approximation we want to study a two level system interacting with a single mode field inside a cavity. For this, we first denote the two levels of our system as the ground state $|g\rangle$ and excited state $|e\rangle$. The Hamiltonian of the two level atom has the form

$$\hat{H}_{\text{atom}} = E_g|g\rangle\langle g| + E_e|e\rangle\langle e| = \frac{1}{2}\left(E_g + E_e\right)\hat{\mathbb{I}} + \frac{1}{2}\left(E_e - E_g\right)\hat{\sigma}_z \tag{2.33}$$

with E_g the ground state energy, E_e the excited state energy and $\hat{\sigma}_z = |e\rangle\langle e| - |g\rangle\langle g|$ the z-Pauli matrix. If we now denote the energy difference $E_e - E_g$ as $\hbar\omega_a$, where ω_a is the atomic transition frequency, and discard the constant energy term, since it only shifts the total energy by a constant and does not affect the dynamics, we get

$$\hat{H}_{\text{atom}} = \frac{1}{2}\hbar\omega_a\hat{\sigma}_z \tag{2.34}$$

For the field we consider coupling to a single mode in the Schrödinger picture with an arbitrary polarization vector ϵ:

$$\hat{\mathbf{E}} = i\sqrt{\frac{\hbar\omega}{2\epsilon_0 V}}\epsilon\left(\hat{a} + \hat{a}^\dagger\right) \tag{2.35}$$

with the Heisenberg picture operators $\hat{a}(t) = \hat{a}e^{-i\omega t}$, $\hat{a}^\dagger(t) = \hat{a}^\dagger e^{i\omega t}$.

The free Hamiltonian in this case is

$$\hat{H}_0 = \hat{H}_{\text{field}} + \hat{H}_{\text{atom}} = \hbar\omega\hat{a}^\dagger\hat{a} + \frac{1}{2}\hbar\omega_a\hat{\sigma}_z \tag{2.36}$$

where the zero-point energy has been dropped again since it does not contribute to the dynamics. For the interaction Hamiltonian in the dipole approximation (2.32) we have

$$\hat{H}_{\text{int}} = -\hat{d}\cdot\hat{E} = -i\sqrt{\frac{\hbar\omega}{2\epsilon_0 V}}(\hat{d}\cdot\epsilon)\left(\hat{a} + \hat{a}^\dagger\right) \tag{2.37}$$

Expanding $\hat{d}$ in the basis $\{|g\rangle, |e\rangle\}$ gives us

$$\begin{aligned}\hat{d} = \langle g|\hat{d}|g\rangle|g\rangle\langle g| + \langle g|\hat{d}|e\rangle|g\rangle\langle e| + \langle e|\hat{d}|g\rangle|e\rangle\langle g| + \langle e|\hat{d}|e\rangle|e\rangle\langle e| = \\ = d\cdot|g\rangle\langle e| + d^*\cdot|e\rangle\langle g| = d\cdot(\hat{\sigma}_- + \hat{\sigma}_+)\end{aligned} \tag{2.38}$$

where we assume no permanent dipole $\langle g|\hat{d}|g\rangle = \langle e|\hat{d}|e\rangle = 0$ and a real matrix element $d = \langle g|\hat{d}|e\rangle$. The atomic transition operators are defined as

$$\hat{\sigma}_- = |g\rangle\langle e|, \quad \hat{\sigma}_+ = |e\rangle\langle g| \tag{2.39}$$

Then the interaction Hamiltonian (2.37) takes the form

$$\hat{H}_{\text{int}} = \hbar g \left(\hat{\sigma}_- + \hat{\sigma}_+\right)\left(\hat{a} + \hat{a}^\dagger\right) \tag{2.40}$$

with $\hbar g = -i\sqrt{\frac{\hbar\omega}{2\epsilon_0 V}}(d \cdot \epsilon)$

Combining the terms for the free (2.36) and interaction (2.40) Hamiltonians gives us the full Hamiltonian in the Schrödinger picture

$$\begin{aligned} \hat{H} &= \hat{H}_0 + \hat{H}_{\text{int}} = \hat{H}_{\text{field}} + \hat{H}_{\text{atom}} + \hat{H}_{\text{int}} \\ \rightarrow \hat{H} &= \hbar\omega\hat{a}^\dagger\hat{a} + \frac{1}{2}\hbar\omega_a\hat{\sigma}_z + \hbar g\left(\hat{\sigma}_- + \hat{\sigma}_+\right)\left(\hat{a} + \hat{a}^\dagger\right) \end{aligned} \tag{2.41}$$

In the interaction picture the ladder and atomic operators evolve as

$$\begin{aligned} \hat{a}(t) = \hat{a}e^{-i\omega t},\ \hat{a}^\dagger(t) = \hat{a}^\dagger e^{i\omega t} \\ \hat{\sigma}_-(t) = \hat{\sigma}_- e^{-i\omega_a t},\ \hat{\sigma}_+(t) = \hat{\sigma}_+ e^{i\omega_a t} \end{aligned} \tag{2.42}$$

The interaction Hamiltonian (2.40) then takes the form

$$\hat{H}_{\text{int}} = \hbar g\left(\hat{\sigma}_-\hat{a}e^{-i(\omega+\omega_a)t} + \hat{\sigma}_-\hat{a}^\dagger e^{i(\omega-\omega_a)t} + \hat{\sigma}_+\hat{a}e^{-i(\omega-\omega_a)t} + \hat{\sigma}_+\hat{a}^\dagger e^{i(\omega+\omega_a)t}\right) \tag{2.43}$$

For $\omega \approx \omega_a$, the first and last terms with frequencies $\pm(\omega+\omega_a)$ are fast-rotating, as they vary much more rapidly than the other two. Moreover, these terms do not conserve energy. The term $\hat{\sigma}_+(t)\hat{a}^\dagger(t)$ corresponds to the simultaneous excitation of the atom and creation of a photon ($|g\rangle \rightarrow |e\rangle$), while $\hat{\sigma}_-(t)\hat{a}(t)$ corresponds to de-excitation and photon absorption ($|e\rangle \rightarrow |g\rangle$). The interaction Hamiltonian contains terms oscillating at both slow ($\omega-\omega_a$) and fast ($\omega+\omega_a$) frequencies. The fast components represent non-resonant processes that rapidly average out over time and can be neglected under the rotating wave approximation (RWA), which is valid when the coupling strength is small compared to the transition frequencies. Applying the RWA, we drop the fast-rotating, non-energy-conserving terms, and the full Hamiltonian (2.41) in the Schrödinger picture simplifies to

$$\hat{H}_{\text{JC}} = \hbar\omega\hat{a}^\dagger\hat{a} + \frac{1}{2}\hbar\omega_a\hat{\sigma}_z + \hbar g\left(\hat{\sigma}_+\hat{a} + \hat{\sigma}_-\hat{a}^\dagger\right) \tag{2.44}$$

which is called the Jaynes-Cummings Hamiltonian [18]. A schematic representation of this interaction is shown in figure 2.2, illustrating the exchange of energy between

a two-level system and a single quantized cavity mode, as described by the Jaynes–Cummings Hamiltonian (2.44).

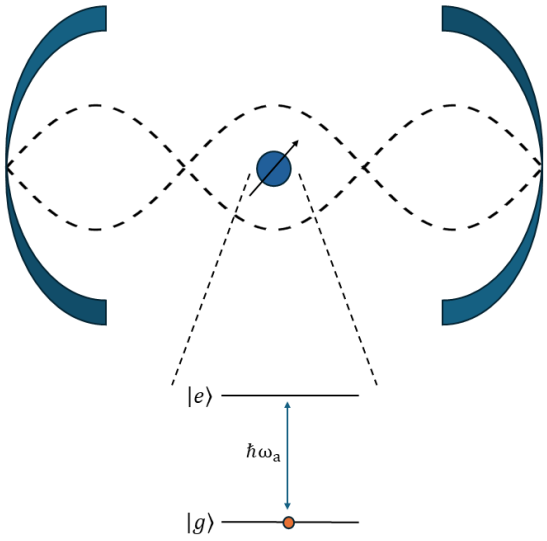

Figure 2.2: Schematic of the Jaynes–Cummings model. A two-level system with ground state $|g>$ and excited state $|e>$ interacts with a single quantized mode of an electromagnetic cavity.

The interaction Hamiltonian $\hat{H}_{\text{int}} = \hbar g \left(\hat{\sigma}_+ \hat{a} + \hat{\sigma}_- \hat{a}^\dagger\right)$ can only cause transitions of the type $|e\rangle|n\rangle \longleftrightarrow |g\rangle|n+1\rangle$ where the product states $|e\rangle|n\rangle$ and $|g\rangle|n+1\rangle$ are the so-called bare states. For a fixed number of photons in the cavity n, the Hamiltonian $\hat{H}_{JC}$ has the eigenvalues (see Appendix A.2)

$$E_\pm = \hbar\omega \left(n + \frac{1}{2}\right) \pm \frac{\hbar}{2}\Omega_n(\Delta) \tag{2.45}$$

where $\Delta = \omega - \omega_a$ is the detuning and $\Omega_n(\Delta) = \sqrt{4g^2\,(n+1) + \Delta^2}$. The eigenvectors associated with these eigenenergies are the dressed states (see also Appendix A.2):

$$\begin{aligned} |n,+\rangle &= \sin\left(\frac{\theta_n}{2}\right)|e,n\rangle + \cos\left(\frac{\theta_n}{2}\right)|g,n+1\rangle \\ |n,-\rangle &= \cos\left(\frac{\theta_n}{2}\right)|e,n\rangle - \sin\left(\frac{\theta_n}{2}\right)|g,n+1\rangle \end{aligned} \tag{2.46}$$

where $\theta_n = \tan^{-1}\left(\frac{2g\sqrt{n+1}}{\Delta}\right)$. The coefficients of the bare states are given by

$$\sin\left(\frac{\theta_n}{2}\right) = \frac{1}{\sqrt{2}}\left[\frac{\Omega_n(\Delta)-\Delta}{\Omega_n(\Delta)}\right]^{\frac{1}{2}}$$
$$\cos\left(\frac{\theta_n}{2}\right) = \frac{1}{\sqrt{2}}\left[\frac{\Omega_n(\Delta)+\Delta}{\Omega_n(\Delta)}\right]^{\frac{1}{2}} \tag{2.47}$$

These eigenstates are known as dressed states, as they represent coherent superpositions of the bare atom-photon states $|e,n\rangle$ and $|g,n+1\rangle$. Unlike the bare states, which describe an uncoupled atom and field, the dressed states incorporate the interaction and describe the true eigenstates of the coupled system. The energy splitting between the dressed states on resonance ($\Delta = 0$) according to equation (2.45) is

$$E_+ - E_- = \hbar\Omega_n(0) = 2\hbar g\sqrt{n+1} \tag{2.48}$$

In figure 2.3 the calculated energies of the Jaynes-Cummings Hamiltonian for $n = 0$ are shown for two different coupling strengths, $g_1 = 0.05\,\hbar\omega$ and $g_2 = 0.1\,\hbar\omega$. The x-axis displays the ratio ω_a/ω, where ω is the fixed cavity frequency. Energies are plotted in units of $\hbar\omega$, and the increasing separation between the dressed states E_+ and E_- with larger g reflects the dependence predicted by equation (2.48).

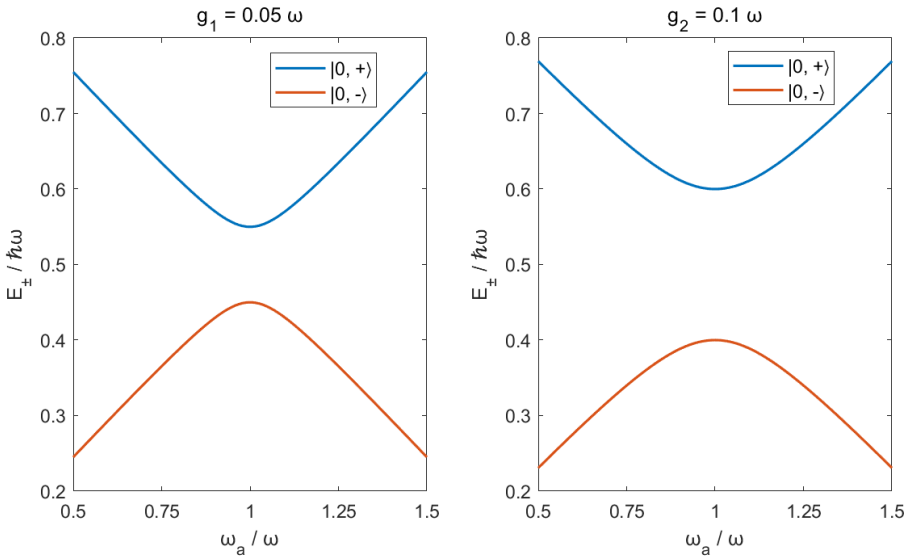

Figure 2.3: Calculated energies of the Jaynes-Cummings Hamiltonian for $n = 0$ in units of $\hbar\omega$ for two different coupling strengths g. We see that for a higher g the energy splitting between E_+ and E_- at zero detuning becomes larger according to equation (2.48).

This means that the interaction between the atom and the single-mode field further splits the bare state energies $E_e = \hbar\frac{\omega_a}{2} + \hbar n\omega$ and $E_g = -\hbar\frac{\omega_a}{2} + \hbar(n+1)\omega$, as illustrated in figure 2.4. The coupling lifts the degeneracy between the two states, leading to a pair of new eigenstates (the so-called dressed states) which are coherent superpositions of the atom being excited with n photons in the field and the atom being in the ground state with $n + 1$ photons. This hybridization between matter and light is one of the central insights of the Jaynes–Cummings model.

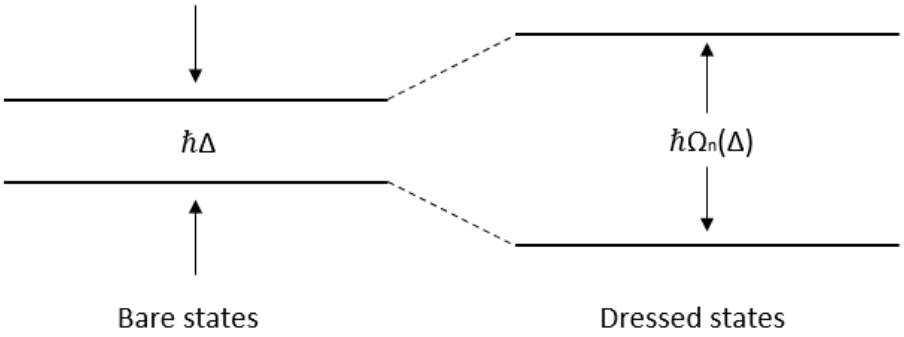

Figure 2.4: The interaction between the atom and the single mode quantized field further splits the bare states in energy.

In the case of resonance ($\Delta = 0$) the bare states $|e, n\rangle$ and $|g, n + 1\rangle$ are degenerate and the splitting between the dressed states scales with $\sqrt{n}$ as can be seen from equation (2.48). This nonlinearity, where the energy spacing between dressed states changes with n, is a key feature of the Jaynes-Cummings model. In contrast to a classical harmonic oscillator, where levels are equally spaced, the $\sqrt{n}$-dependence leads to anharmonic energy gaps. This effect is important in systems like circuit QED, where it allows selective control of individual transitions and plays a role in phenomena such as photon blockade [19]. The so-called Jaynes-Cummings ladder is shown in figure 2.5.

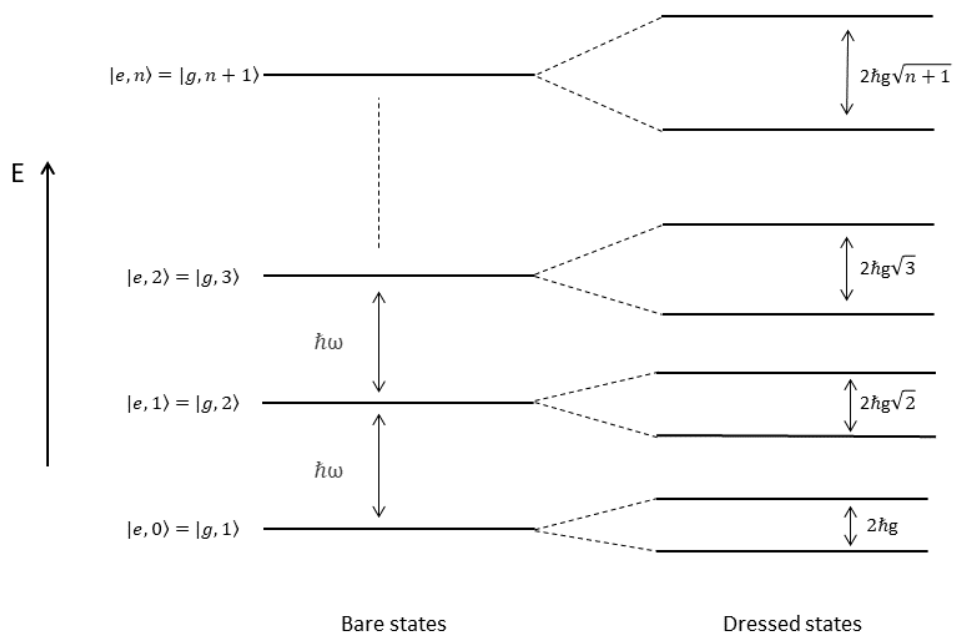

Figure 2.5: Jaynes-Cummings ladder: for zero detuning Δ the bare states are degenerate and the splitting between the dressed states scales with $\sqrt{n}$.

One can also shift the energy levels such that the ground state of the atom has 0 energy. The atomic Hamiltonian now takes the form

$$\hat{H}_{\text{atom}} = E_e|e\rangle\langle e| = \hbar\omega_a\hat{\sigma}_+\hat{\sigma}_- \tag{2.49}$$

The energy shifted Jaynes-Cummings Hamiltonian now reads

$$\hat{H}_{JC} = \hbar\omega\hat{a}^\dagger\hat{a} + \hbar\omega_a\hat{\sigma}_+\hat{\sigma}_- + \hbar g\left(\hat{\sigma}_+\hat{a} + \hat{\sigma}_-\hat{a}^\dagger\right) \tag{2.50}$$

and the new eigenvalues of the full Hamiltonian are shifted in energy (see Appendix A.3):

$$E_\pm = \hbar\omega\left(n + \frac{1}{2}\right) + \frac{1}{2}\hbar\omega_a \pm \frac{\hbar}{2}\Omega_n(\Delta) \tag{2.51}$$

This energy shift does not alter the physical behavior of the system, but it simplifies the mathematical form of the Hamiltonian by setting the ground state energy to zero. It is often convenient in cavity QED to redefine the energy scale in this way, especially when comparing models or calculating transition energies. The resulting eigenvalues maintain the same avoided crossing structure as before, with an energy

splitting that depends on the coupling strength g. In figure 2.6 the energies of the shifted Jaynes-Cummings Hamiltonian for $n = 0$ and two different coupling strengths $g_1 = 0.05\,\hbar\omega$, $g_2 = 0.1\,\hbar\omega$ is shown as a function of the detuning $\Delta = \omega - \omega_a$.

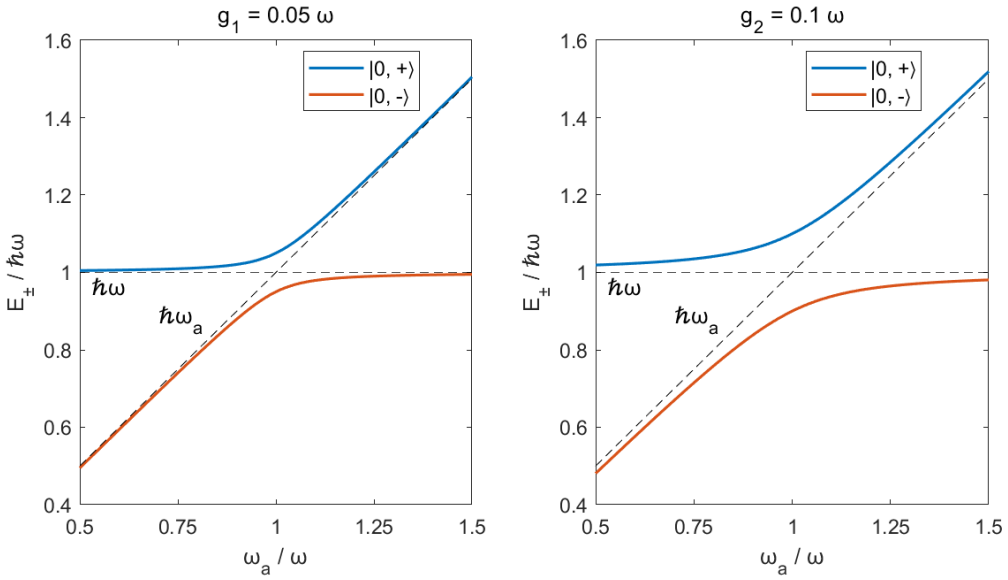

Figure 2.6: Calculated energies of the shifted Jaynes-Cummings Hamiltonian for $n = 0$ in units of $\hbar\omega$ for two different coupling strengths g. The avoided crossing between E_+ and E_- at $\Delta = 0$ results at an energy splitting, which is again equal to $2\hbar g$, as was before introducing the energy shift.

2.1.3 Rabi Oscillations

In order to obtain the dynamics described by the Jaynes-Cummings Hamiltonian for an arbitrary initial state let us consider the Hamiltonian (2.50) in the interaction picture according to the equations [16]

$$\begin{aligned} \hat{H}_{\text{int}}(t) &= e^{\frac{i}{\hbar}\hat{H}_0 t}\hat{H}_{\text{int}}e^{\frac{-i}{\hbar}\hat{H}_0 t} \\ |\psi_{\text{int}}(t)\rangle &= e^{\frac{i}{\hbar}\hat{H}_0 t}|\psi(t)\rangle \end{aligned} \tag{2.52}$$

where $\hat{H}_0$ is the free Hamiltonian, i.e. the sum of the radiation field and atomic parts and $\hat{H}_{\text{int}}$ the interaction part of the full Hamiltonian in the Schrödinger picture. For the interaction Hamiltonian one then gets (see Appendix A.4):

$$\hat{H}_{\text{int}}(t) = \hbar g\left(\hat{\sigma}_+\hat{a}e^{-i\Delta t} + \hat{\sigma}_-\hat{a}^\dagger e^{i\Delta t}\right) \tag{2.53}$$

The Schrödinger equation in the interaction picture then is

$$i\hbar\frac{\partial}{\partial t}|\psi_{\text{int}}(t)\rangle = \hat{H}_{\text{int}}(t)|\psi_{\text{int}}(t)\rangle \tag{2.54}$$

We now make an ansatz assuming that the state vector can be written as a superposition between the bare states $|e,n\rangle$ and $|g,n+1\rangle$ as

$$|\psi_{\text{int}}(t)\rangle = \sum_n c_{e,n}(t)|e,n\rangle + c_{g,n+1}(t)|g,n+1\rangle \tag{2.55}$$

Inserting this ansatz into the Schrödinger equation (2.54) we get a system of coupled differential equations for the bare state coefficients:

$$\begin{aligned}\dot{c}_{e,n}(t) &= -ig\sqrt{n+1}e^{-i\Delta t}c_{g,n+1}(t)\\ \dot{c}_{g,n+1}(t) &= -ig\sqrt{n+1}e^{i\Delta t}c_{e,n}(t)\end{aligned} \tag{2.56}$$

If we now assume no detuning and the system being in the initial state $|e,n\rangle : c_{e,n}(0) = 1, c_{g,n+1}(0) = 0$ we get the solutions

$$\begin{aligned}c_{e,n}(t) &= \cos\left(gt\sqrt{n+1}\right)\\ c_{g,n+1}(t) &= -i\sin\left(gt\sqrt{n+1}\right)\end{aligned} \tag{2.57}$$

The probabilities for the two states then are

$$\begin{aligned}P_{e,n}(t) = |c_{e,n}(t)|^2 &= \frac{1}{2}\left[1+\cos\left(\Omega_n t\right)\right]\\ P_{g,n+1}(t) = |c_{g,n+1}(t)|^2 &= \frac{1}{2}\left[1-\cos\left(\Omega_n t\right)\right]\end{aligned} \tag{2.58}$$

with $\Omega_n = 2g\sqrt{n+1}$ and the atomic inversion

$$W(t) = P_{e,n}(t) - P_{g,n+1}(t) = \cos\left(\Omega_n t\right) \tag{2.59}$$

These solutions show that the system undergoes constant oscillations between the states $|e,n\rangle \longleftrightarrow |g,n+1\rangle$, known as Rabi oscillations, with the Rabi frequency Ω_n. One can

notice that even in the absence of cavity photons, i.e. when $n = 0$, we still have vacuum Rabi oscillations with the Rabi frequency $\Omega_0 = 2g$. This indicates that even the vacuum can trigger the continuous excitation exchange between the atom and the radiation field. In this case the atom can spontaneously emit a photon and then reabsorb it. These oscillations represent the coherent energy exchange between the atom and the quantized field mode of the cavity. The periodicity reflects the reversibility of the interaction under ideal conditions, with no dissipation or detuning. The dependence of Ω_n on $\sqrt{n+1}$ reflects the discrete photon-number dependence of the fully quantum description. In contrast, a semiclassical treatment with a classical drive leads to a Rabi frequency that depends on the field amplitude, but does not predict oscillations in the absence of photons. Figure 2.7 illustrates these Rabi oscillations of the atomic inversion $W(t)$ for the case where $n = 0$.

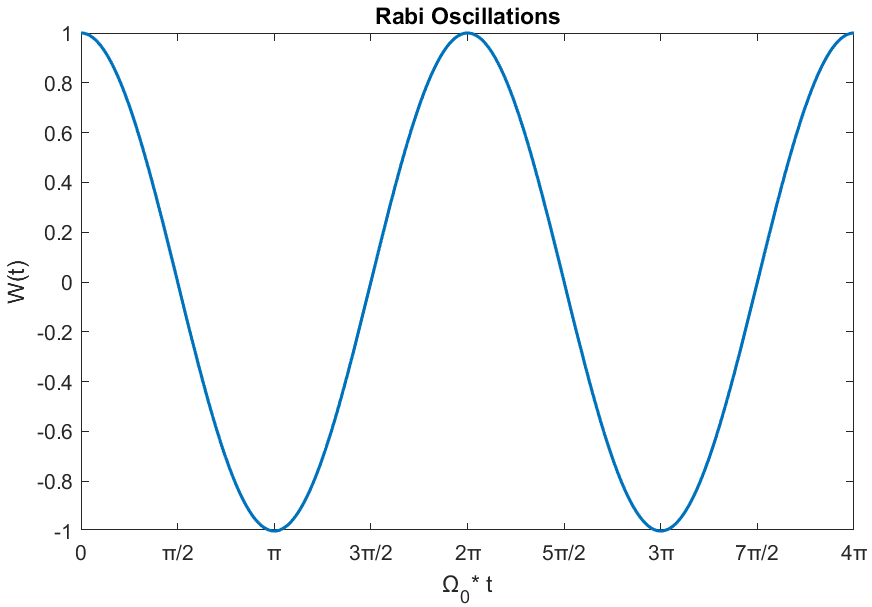

Figure 2.7: Rabi oscillations for the case $n = 0$ and no detuning ($\Delta = 0$) with the Rabi frequency $\Omega_0 = 2g$. The system starts in the state $|e, 0\rangle$ where the atom is in the excited state and we have 0 photons in the cavity. After time $\frac{\pi}{\Omega_0}$ there is a unit probability of finding the atom in the ground state, having emitted a single photon into the cavity, resulting in the state $|g, 1\rangle$.

2.1.4 Tavis-Cummings Hamiltonian

The Tavis-Cummings Hamiltonian [20] is a generalization of the Jaynes-Cummings Hamiltonian for multiple two-level systems. In the literature, these two-level systems are often referred to as "spins" since a two-level system is mathematically equivalent to a spin-$\frac{1}{2}$ particle. While the Jaynes-Cummings model describes the interaction of a single spin with a single radiation mode, the Tavis-Cummings model describes the interaction of an ensemble of such spins with a single radiation mode. This many-spin description is essential for modeling our system, where a large ensemble of sodium atoms simultaneously interacts with a single cavity mode (see Chapter 3). Since each individual spin couples weakly to the resonator, only the collective interaction, captured by the Tavis–Cummings model, leads to a strong enough coupling strength to observe coherent dynamics. The model thus forms the theoretical foundation for understanding the collective behavior we observe in our experiment.

As with the Jaynes-Cummings model (figure 2.2), a schematic representation of this many-body interaction is shown in figure 2.8. It depicts an ensemble of two-level systems collectively coupled to a single mode of a quantized electromagnetic field in a cavity. Each spin interacts with the cavity mode via the same coupling mechanism as in the Jaynes–Cummings model.

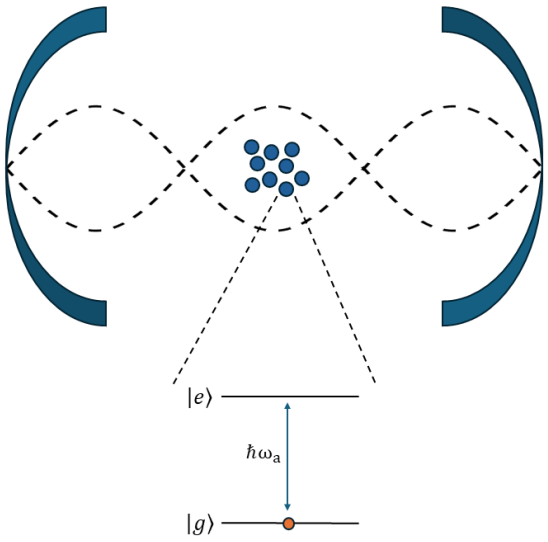

Figure 2.8: Schematic of the Tavis–Cummings model. An ensemble of N identical two-level systems (spins) couples to a single mode of a quantized electromagnetic cavity field. The interaction is described by collective spin operators, resulting in phenomena such as collective coupling enhancement and Dicke states.

In our earlier derivation, the coupling was described in terms of an electric dipole interaction. In our experiment, however, the coupling is magnetic in nature, the spins

couple to the magnetic field of the microwave resonator. Despite this physical difference, the underlying Hamiltonian has the same mathematical form.

In order to get the Tavis-Cummings Hamiltonian we can generalize the Jaynes-Cummings Hamiltonian to include multiple spins, each with different frequency ω_a^i and coupling strength g_i:

$$\hat{H}_{TC} = \hbar\omega\hat{a}^\dagger\hat{a} + \frac{1}{2}\sum_{i=1}^{N}\hbar\omega_a^i\hat{\sigma}_z^i + \sum_{i=1}^{N}\hbar g_i\left(\hat{\sigma}_+^i\hat{a} + \hat{\sigma}_-^i\hat{a}^\dagger\right) \tag{2.60}$$

where N is the number of spins. This Hamiltonian describes the energy of an ensemble of spins which are inhomogeneously broadened, meaning each spin has a different transition frequency, and also have a different coupling strength to the cavity mode. If we now make a simplifying assumption that all spins have the same transition frequency $\omega_a^i = \omega_a$ and the same coupling strength $g_i = g$, we can introduce the collective spin operators

$$\begin{aligned}\hat{S}_z &= \sum_{i=1}^{N}\hat{\sigma}_z^i \\ \hat{S}_\pm &= \frac{1}{\sqrt{N}}\sum_{i=1}^{N}\hat{\sigma}_\pm^i\end{aligned} \tag{2.61}$$

in order to simplify the Hamiltonian to:

$$\hat{H}_{TC} = \hbar\omega\hat{a}^\dagger\hat{a} + \frac{1}{2}\hbar\omega_a\hat{S}_z + \hbar g_{\text{coll}}\left(\hat{S}_-\hat{a} + \hat{S}_+\hat{a}^\dagger\right) \tag{2.62}$$

where the collective coupling to the cavity mode g_{coll} arises from the combined contribution of each individual spin. This collective coupling strength, represents the total effect of all spins interacting with the cavity mode as

$$g_{\text{coll}} = \sqrt{g_1^2 + g_2^2 + g_3^2 + ...} = \sqrt{N}\cdot g \tag{2.63}$$

The eigenenergies of the system (2.62) are similar to the single spin case:

$$E_\pm = \hbar\omega\left(n + \frac{1}{2}\right) \pm \frac{\hbar}{2}\Omega_n(\Delta) \tag{2.64}$$

with $\Omega_n(\Delta) = \sqrt{4g_{\text{coll}}^2(n+1) + \Delta^2}$.

For the case $n = 0$ we get the eigenstates

$$|\pm\rangle = \frac{1}{\sqrt{2}} \left(|1, G\rangle \pm |0, D_1\rangle \right) \tag{2.65}$$

where $|G\rangle$ is the collective ground state for N spins: $|G\rangle = |g\rangle|g\rangle|g\rangle|g\rangle...|g\rangle$ and $|D_1\rangle$ is the (first) Dicke state [9], which is a state with all spins down except one, i.e. one excitation, equally shared as a superposition state among all spins:

$$|D_1\rangle = \frac{1}{\sqrt{N}} \left(|e\rangle|g\rangle|g\rangle...|g\rangle + |g\rangle|e\rangle|g\rangle...|g\rangle + ... + |g\rangle|g\rangle|g\rangle...|e\rangle \right) \tag{2.66}$$

Note however, these are not the only eigenstates since we deal with a larger Hilbert space in this case, which describes more than one spin. We can further extend the Tavis-Cummings Hamiltonian by considering an extra term which describes the case of driving the cavity with an external classical field:

$$\hat{H}_p = i\hbar\eta \left(\hat{a}^\dagger e^{-i\omega_d t} - \hat{a} e^{i\omega_d t} \right) \tag{2.67}$$

with η being the amplitude of the drive. This results in the driven Tavis-Cummings Hamiltonian:

$$\hat{H}_{TC} = \hbar\omega \hat{a}^\dagger \hat{a} + \frac{1}{2} \sum_{i=1}^{N} \hbar\omega_a^i \hat{\sigma}_z^i + \sum_{i=1}^{N} \hbar g_i \left(\hat{\sigma}_+^i \hat{a} + \hat{\sigma}_-^i \hat{a}^\dagger \right) + i\hbar\eta \left(\hat{a}^\dagger e^{-i\omega_d t} - \hat{a} e^{i\omega_d t} \right) \tag{2.68}$$

We can further simplify this Hamiltonian by getting rid of the time dependency using a unitary transformation of the form

$$\hat{U} = e^{-i\omega t \left(\hat{a}^\dagger \hat{a} + \sum_i \frac{\sigma_z^i}{2} \right)} \tag{2.69}$$

resulting in the Hamiltonian (see [21]):

$$\hat{H}_{TC} = \hbar\Delta_c \hat{a}^\dagger \hat{a} + \frac{1}{2} \sum_{i=1}^{N} \hbar\Delta_s^i \hat{\sigma}_z^i + \sum_{i=1}^{N} \hbar g_i \left(\hat{\sigma}_+^i \hat{a} + \hat{\sigma}_-^i \hat{a}^\dagger \right) + i\hbar\eta \left(\hat{a}^\dagger - \hat{a} \right) \tag{2.70}$$

where $\Delta_c = \omega_c - \omega_d$ is the frequency detuning between cavity and drive and $\Delta_s^i = \omega_s^i - \omega_d$ being the frequency detuning between the corresponding spin (i) and the drive.

2.1.5 Open Quantum Systems - Maxwell-Bloch Equations

So far, the Tavis-Cummings Hamiltonian describes an ideal, isolated system composed of a cavity mode coupled to a spin ensemble. However, in real experimental settings, interactions with the environment must be considered. These include energy loss from the cavity and decoherence in the spin system as a result of spin-spin interactions and coupling to phonons or other bath modes. To capture these effects, we treat the system as an open quantum system.

The standard formalism for describing open quantum systems is the Lindblad master equation [22], which adds dissipative terms to the von Neumann evolution of the density matrix $\hat{\rho}$:

$$\frac{d\hat{\rho}}{dt} = -\frac{i}{\hbar}[\hat{H}, \hat{\rho}] + \hat{\mathcal{L}}[\hat{\rho}] \tag{2.71}$$

where $\hat{\mathcal{L}}[\hat{\rho}]$ is the Liouvillian superoperator incorporating dissipation. The Liouvillian superoperator accounts for all decoherence processes and is composed of three dissipators as [22]:

$$\begin{aligned}\hat{\mathcal{L}}[\hat{\rho}] = \kappa &\left(2\hat{a}\hat{\rho}\hat{a}^\dagger - \hat{a}^\dagger\hat{a}\hat{\rho} - \hat{\rho}\hat{a}^\dagger\hat{a}\right) \\ &+ \frac{\gamma_\parallel}{2}\sum_j \left(2\hat{\sigma}_-^j\hat{\rho}\hat{\sigma}_+^j - \hat{\sigma}_+^j\hat{\sigma}_-^j\hat{\rho} - \hat{\rho}\hat{\sigma}_+^j\hat{\sigma}_-^j\right) \\ &+ \frac{\gamma_\perp}{2}\sum_j \left(\hat{\sigma}_z^j\hat{\rho}\hat{\sigma}_z^j - \hat{\rho}\right)\end{aligned} \tag{2.72}$$

The first term describes photon loss in the cavity mode $\hat{a}$ due to damping at a rate κ. This cavity loss rate accounts for energy leakage through imperfect mirrors, coupling to the transmission line, or internal losses, and it determines the linewidth of the resonance. The second term describes spin relaxation, which may arise from spontaneous emission or spin-phonon interactions, with the coupling operator $\hat{\sigma}_-$, occurring at a rate $\gamma_\parallel = 1/T_1$. The third term describes dephasing due to spin-spin and spin-bath interactions, modeled with the operator $\hat{\sigma}_z$ and occurs at a rate $\gamma_\perp = 1/T_2$. Here, T_1 and T_2 are the longitudinal relaxation and transverse dephasing times [23], respectively, which are introduced in more detail in section 2.2.

The equations of motion can then be calculated as shown below (2.73). In obtaining these equations, products of operators such as $\langle\hat{a}^\dagger\hat{\sigma}_-^j\rangle$ were factorized into $\langle\hat{a}^\dagger\rangle\langle\hat{\sigma}_-^j\rangle$, and similarly for other terms. This semiclassical approximation neglects quantum correlations between the cavity field and individual spins, which is well justified in the limit of a large spin ensemble and weak single-spin coupling.

$$\begin{aligned}
\langle \dot{\hat{a}} \rangle &= -i\Delta_c \langle \hat{a} \rangle + \sum_j g_j \langle \hat{\sigma}_-^j \rangle + \eta - \kappa \langle \hat{a} \rangle \\
\langle \hat{\sigma}_-^j \rangle &= -i\Delta_s^j \langle \hat{\sigma}_-^j \rangle + g_j \langle \hat{a} \rangle \langle \hat{\sigma}_z^j \rangle - \left(\frac{\gamma_\parallel}{2} + \gamma_\perp \right) \langle \hat{\sigma}_-^j \rangle \\
\langle \dot{\hat{\sigma}}_z^j \rangle &= -2g_j \left(\langle \hat{a}^\dagger \rangle \langle \hat{\sigma}_-^j \rangle + \langle \hat{a} \rangle \langle \hat{\sigma}_+^j \rangle \right) - \gamma_\parallel \left(1 + \langle \hat{\sigma}_z^j \rangle \right)
\end{aligned} \tag{2.73}$$

These are known as the Maxwell–Bloch equations. For a detailed derivation in the context of our experiment, see [21, 23].

As discussed earlier, the transition frequencies of the individual spins are not identical but rather exhibit a spread, commonly referred to as inhomogeneous broadening. A suitable way to model the spin frequency distribution in solid-state spin systems is the q-Gaussian distribution (Tsallis distribution) [24]:

$$\rho(\omega) = \left(1 - (1-q) \frac{(\omega - \omega_0)^2}{\delta^2} \right)^{\frac{1}{1-q}} \tag{2.74}$$

with $\delta = \frac{\gamma_q}{2\sqrt{(2^q-2)/(2q-2)}}$, where γ_q is the full width at half maximum (FWHM). The parameter $1 < q < 3$ controls the shape of the distribution, specifically how fast the tails of the distribution fall off. For $q \to 1$, the function reduces to a standard Gaussian, for $q > 1$, it exhibits heavier tails, decaying more slowly than a Gaussian, and increasingly approaches a Lorentzian as $q = 2$.

A key condition for observing coherent exchange between the resonator and the spin ensemble, before excitations are lost through decoherence or excitation loss, is to operate in the strong coupling regime. This condition is met when the collective coupling strength $g_{\text{coll}} = \sqrt{N} \cdot g$ exceeds both the cavity decay rate κ and the ensemble's effective decoherence rate Γ, i.e., $g_{\text{coll}} > \kappa, \Gamma$. In this regime, energy can be coherently exchanged between the spin ensemble and the cavity mode faster than it is dissipated to the environment. In the absence of inhomogeneous broadening, the relevant decoherence rate Γ is simply the transverse relaxation rate $\gamma_\perp = 1/T_2$. However, for inhomogeneously broadened spin ensembles, this is no longer accurate. The effective linewidth Γ includes both the intrinsic single spin decoherence $\gamma_\perp$ and the spread (FWHM) in resonance frequencies across the ensemble γ_q. As shown in [11, 25], Γ can be obtained from a convolution of the inhomogeneous frequency distribution with the single spin linewidth as

$$\Gamma = \left[\int_{-\infty}^{\infty} \frac{\rho(\omega)\, d\omega}{\gamma_\perp + \mathrm{i}(\omega - \omega_0)} \right]^{-1} \tag{2.75}$$

A useful factor in this context is the cooperativity $C = \frac{g_{\text{coll}}^2}{\kappa\Gamma}$, which quantifies the

ratio of coherent interaction strength to dissipative losses. Strong coupling corresponds to $C > 1$.

In the steady-state regime, relevant for fitting measurements of transmission spectra of our resonator with a Vector Network Analyzer (VNA) (see 3.1.2), the time derivatives in equation (2.73) vanish. Assuming the spins are initially in their ground state, $\langle \hat{\sigma}_z^j \rangle = -1$, and that the system is weakly driven, one obtains the following expression for the cavity amplitude [23]:

$$\langle \hat{a} \rangle = \frac{\eta}{i\Delta_c + \kappa + g^2 \sum_j \frac{\rho_j}{\gamma_\perp + \frac{\gamma_\parallel}{2} + i\Delta_s^j}} \tag{2.76}$$

To calculate the transmission spectrum (for later comparison with the experiment), we discretize the spin frequency distribution (2.74) into N_p spin packets with equal spacing. Each of the N_p numerical spins, indexed by j, couples to the cavity with coupling strength $g = g_{\text{coll}}/\sqrt{N_p}$ and is weighted by discrete weights $\rho_j = \rho(\omega_j)$, which are normalized as $\sum_j \rho_j = 1$. For more details on the discretization procedure and equation (2.74) see [21, 23]. This steady-state solution will later be used in section 4.1 to fit transmission spectra from magnetic field scans.

2.2 Spin Dynamics

After introducing the theoretical models in the previous section, we now turn to experimental methods for studying the spin dynamics of spin ensembles, particularly focusing on measuring their ability to maintain coherence. Coherence in spin ensembles is limited by two fundamental relaxation mechanisms: longitudinal relaxation and transverse relaxation. The longitudinal relaxation time T_1 describes how quickly the spins return to thermal equilibrium after being excited, due to energy exchange with the surrounding environment (spin-lattice relaxation). This process governs how long spins remain in an excited state before decaying back to the ground state. On the other hand, the transverse relaxation time T_2 characterizes the loss of phase coherence between spins due to interactions within the ensemble and with the environment. In realistic experimental conditions, an additional timescale, T_2^* (inhomogeneous dephasing time), emerges. This timescale is influenced by static field inhomogeneities and variations in the local environment, which shift the exact transition frequencies of individual spins (inhomogeneous broadening) and cause the ensemble to dephase more rapidly than in the ideal case. As a result, T_2^* is generally shorter than the intrinsic T_2 because it accounts for additional sources of dephasing that are not captured by the

ideal T_2 relaxation time.

In the following, we first introduce coherence in spin systems in more detail and then discuss the Hahn echo sequence, a technique for measuring the intrinsic coherence time T_2 by refocusing static dephasing effects. To further extend coherence times, the Carr-Purcell-Meiboom-Gill (CPMG) sequence builds upon the Hahn method by applying multiple refocusing pulses. These additional pulses not only correct for static field variations but also help mitigate the effects of spin-spin interactions and systematic pulse errors. As a result, CPMG allows for more robust and extended measurements of spin coherence under realistic experimental conditions.

2.2.1 Coherence in Spin Systems

In spin ensembles, coherence refers to the ability of individual spins to maintain a well-defined phase during their evolution in response to external electromagnetic fields. This phase stability is crucial for the collective behavior observed in cavity QED experiments. However, interactions with their surrounding environment, such as fluctuations in the local magnetic field, interactions with neighbouring spins, and other sources of noise, lead to a loss of coherence, a process known as decoherence [22, 26]. Decoherence results in the loss of phase information and the decay of the signal amplitude over time.

The characteristic timescale of this decay in an ensemble measurement is typically denoted as T_2^*, known as the inhomogeneous dephasing time. It includes both intrinsic decoherence and static variations in the spin environment, such as slight differences in local magnetic fields or spin transition frequencies. In contrast, the intrinsic coherence time of an individual spin, denoted T_2, quantifies how long the spin maintains phase coherence under the influence of intrinsic relaxation processes, excluding static variations in the local environment. Understanding and characterizing T_2 and T_2^* is essential for evaluating the coherence properties of spin systems and for designing control techniques such as the Hahn echo, which aims to recover the true T_2 by refocusing phase errors.

A helpful way to conceptualize spin dephasing is through the Bloch sphere representation [27, 28]. A pure superposition state such as $\frac{1}{\sqrt{2}}(|g\rangle + |e\rangle)$ corresponds to a Bloch vector lying on the equator of the sphere, perpendicular to the z-axis. In a spin ensemble, small differences in the local environment cause each spin to precess at a slightly different frequency, leading to a gradual loss of phase alignment around the equator. This dephasing process, governed by T_2^*, describes how long a collective superposition state persists before the ensemble coherence vanishes due to phase dispersion. While each individual spin remains in a coherent superposition state, their transverse Bloch vectors become randomly distributed in azimuthal angle, effectively cancelling each other out when summed. Figure 2.9 illustrates the dephasing mechanism associated

with T_2^*. In contrast, the intrinsic T_2 time describes how the transverse component of each individual spin shrinks in length due to interactions with the environment, eventually reducing the spin to a true mixed state.

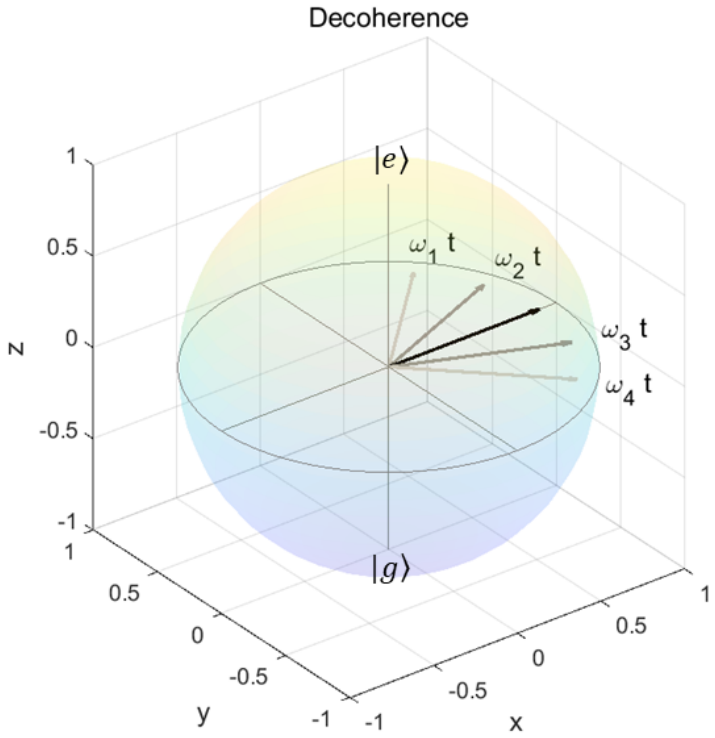

Figure 2.9: Visualization of ensemble dephasing due to inhomogeneous broadening (i.e., T_2^*). Each vector represents a spin in the ensemble, initially aligned in the transverse (xy) plane on the Bloch sphere. Slight variations in local magnetic environments cause each spin to precess at a slightly different frequency ($\omega_1, \omega_2, \ldots$), leading to a gradual fan-out around the equator. This results in the decay of the net transverse magnetization on a timescale T_2^*.

2.2.2 Hahn Echo Method

The Hahn echo sequence [29] is a common technique originally used in nuclear magnetic resonance (NMR) [30], but it is broadly applicable to other types of spin systems, including electronic spin ensembles studied in cavity QED experiments, where it is used to measure the coherence time T_2.

As already mentioned in 2.2.1, inhomogeneously broadened systems contain spins that precess at slightly different rates due to local variations in their environment. This leads to a rapid decay of the collective signal on a timescale T_2^*, even when the intrinsic spin coherence remains high. This effect can be observed experimentally as a free induction decay (FID) signal following a single resonant $\pi/2$ pulse [31]. The FID reflects how the ensemble dephases due to static frequency offsets across the sample.

To isolate the intrinsic transverse relaxation time T_2, one must eliminate the influence of these static inhomogeneities. The Hahn echo technique accomplishes this by inserting a π pulse midway through the spin evolution. This pulse inverts the accumulated phases of the individual spins, causing them to refocus at a later time. As a result, these static differences in spin precession are effectively removed, and the remaining signal decay reveals the intrinsic transverse relaxation time T_2, free from the influence of fixed frequency offsets. The exact procedure of the Hahn echo sequence is shown in figure 2.10.

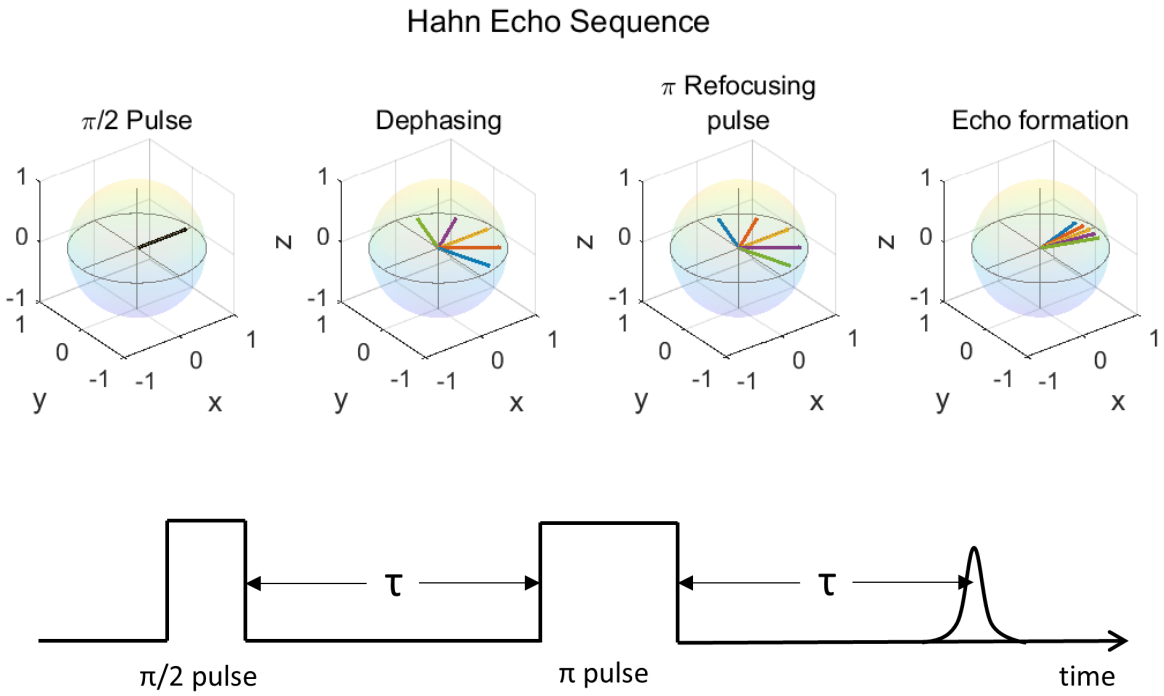

Figure 2.10: Hahn Echo Sequence [29]: All spins start in the ground state. After a $\frac{\pi}{2}$ pulse, the spin ensemble ends up on the equator of the Bloch sphere, i.e., in a superposition of states between $|g\rangle$ and $|e\rangle$ (sphere #1) and the spins start to dephase (sphere #2). The different colors of the spin vectors represent the varying rates at which individual spins precess around the equator due to magnetic field inhomogeneities and local interactions. After dephasing for time τ, a π pulse rotates the spins on the equator, effectively inverting their phases (sphere #3). This enables the spins to refocus over the next time interval τ. At the end of this interval, the spins are fully refocused, producing an echo signal (sphere #4). The Bloch spheres are shown in the rotating frame of the spin center frequency.

The first step is to initialize the spin ensemble in the ground state. In our experiment, this occurs naturally due to thermalization: at millikelvin temperatures, the thermal energy $k_B T$ is much smaller than the spin transition energy $\hbar\omega_a$, so nearly all spins occupy the ground state. As shown in the previous section 2.1.4 one can apply an external drive to the cavity, in our case a microwave pulse, giving us control of the

spin ensemble. The experimental methods on how to initialize the spins and control them by sending microwave pulses into the system will be discussed later in Chapter 3. From this state, with the spin ensemble in the ground state, we apply a $\frac{\pi}{2}$ pulse. This pulse is a microwave burst with a duration $t_{\pi/2}$, defined by the condition $t_{\pi/2} = \frac{\pi}{2\Omega_0}$, where Ω_0 is the effective Rabi frequency. The $\pi/2$ pulse effectively rotates the spins from their initial alignment along the z-axis onto the equatorial xy-plane of the Bloch sphere, creating a superposition state. This is shown in figure 2.7, where it can be seen that applying such a pulse results in $W(t) = 0$, corresponding to an equal probability of the spin being in either of the two states. Immediately afterwards, the spins begin to dephase due to static variations in their local environments, which leads to decoherence across the ensemble. Each individual spin precesses around the z-axis with a different speed, because we are dealing with an inhomogeneously broadened system as discussed earlier 2.1.4. After a time τ we apply a π pulse, or refocusing pulse, which flips the spins from their initial orientation to the opposite one. This effectively applies a rotation of 180° about the x-axis, flipping the spin component $y \rightarrow -y$ on the Bloch sphere. The spins now start to refocuse towards their initial superposition state and after time τ they are fully refocused and a so-called echo signal is produced which one can measure experimentally. The time scale over which this refocusing is possible is limited by the spin transverse relaxation time T_2, because T_2 quantifies the timescale over which the phase coherence of each single spin decays due to interaction with their environment. As time progresses, dephasing causes the spins to lose their ability to refocus and produce a detectable echo signal.

The echo signal provides a way to measure the coherence time T_2 of our system by analyzing the decay of the echo amplitude as a function of the precession time τ. By varying τ, recording the echo signal for each value, and plotting the peak amplitudes, one observes an exponential decay. This decay can be described by a function of the form $e^{-\frac{2\tau}{T_2}}$ where T_2 characterizes the coherence time of the spin ensemble. Figure 2.11 illustrates a representative example of such a decay, showing simulated data points, where each point corresponds to the echo signal for a different precession time τ, along with a fitted exponential curve. From such a fit, the coherence time T_2 can be extracted.

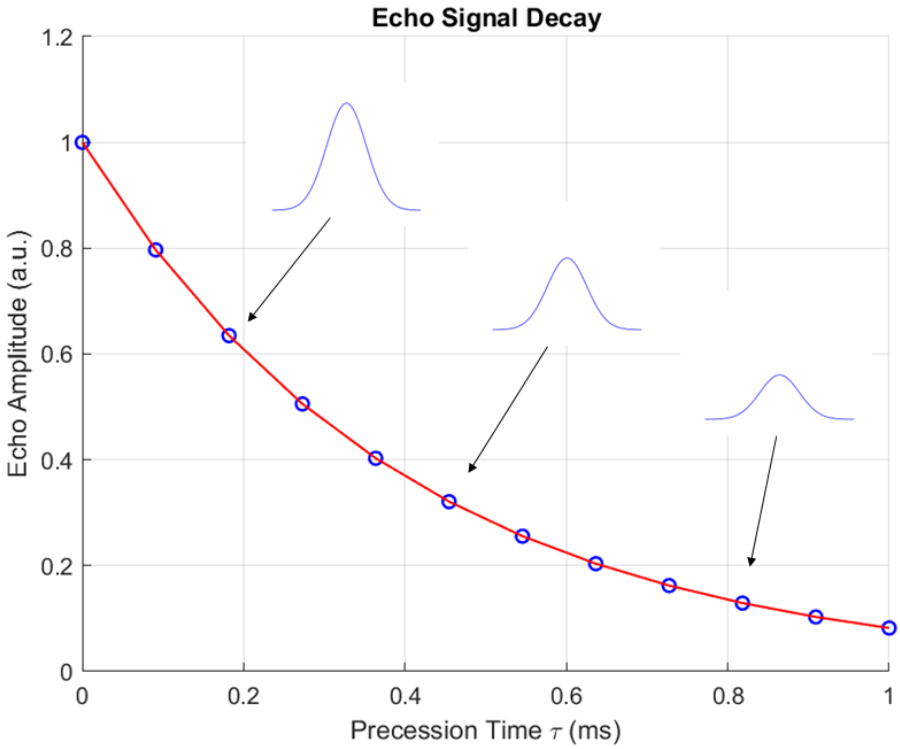

Figure 2.11: Representative decay of the echo signal amplitude as a function of the precession time τ. The data points are simulated to illustrate the expected behavior, while the solid line corresponds to a fit of the exponential decay function $e^{-\frac{2\tau}{T_2}}$, highlighting how the coherence time T_2 is extracted. The decreasing size of the echo peaks with increasing τ illustrates the loss of coherence over time.

2.2.3 Carr-Purcell-Meiboom-Gill Method

Hahn echo sequences are susceptible to many decoherence mechanisms, including environmental factors such as field inhomogeneities and spin-spin interactions within the ensemble, as they rely on a single refocusing pulse to reverse dephasing. Furthermore, in an inhomogeneously broadened spin ensemble, variations in resonance frequencies across the ensemble mean that a single π pulse may not perfectly refocus all spins, as the pulse calibration is optimized for an average frequency rather than individual spins.

Dynamical decoupling sequences exist [32, 33], that are designed to mitigate such limitations by applying a series of carefully timed control pulses that periodically flip the spins, thereby continuously reversing their accumulated phase and refocusing their evolution. This suppresses dephasing from slow environmental fluctuations and extends coherence. Additionally, dynamical decoupling can help supress systematic control errors, such as slight over- or underrotations in pulse amplitude, especially when

combined with clever pulse axis choices, as in the CPMG sequence.

An extension of the Hahn echo is the Carr-Purcell-Meiboom-Gill (CPMG) sequence [34, 35]. The system is again initialized in the ground state and a $\pi/2$ pulse, applied around the x-axis, rotates the spin ensemble onto the equator of the Bloch sphere. We then apply a π pulse around the y-axis after a precession time τ but in this case instead of scanning the time τ we apply a series of π refocusing pulses separated by equal times 2τ resulting in a CPMG train. Because the first $\pi/2$ and subsequent π pulses are applied around orthogonal axes, certain systematic pulse errors can cancel out in pairs. For example, if a π pulse rotates a spin slightly less than 180° (e.g., 170°), the next pulse can compensate for this small error, bringing the spin back to the correct trajectory. This geometric cancellation improves robustness against pulse imperfections.

A decaying echo signal is observed between each consecutive π pulse, as spins rephase after every delay τ and produce an echo peak. One can then fit a curve of the type $e^{\frac{-t}{T_2}}$ to the experimental data and extract the value for the coherence time T_2. The pulse sequence and resulting echo train are illustrated in figure 2.12.

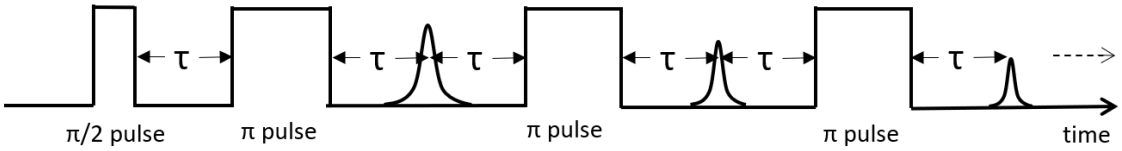

Figure 2.12: CPMG sequence: The spin ensemble is first initialized in the ground state. A $\frac{\pi}{2}$ pulse brings the spins into the transverse plane, creating a superposition state. Unlike the Hahn echo sequence, where a single π pulse is used for refocusing, the CPMG sequence applies a train of π pulses at regular intervals 2τ. Each π pulse inverts the spin phases, leading to a periodic refocusing of the spin ensemble and the formation of multiple echo signals. This repeated refocusing extends the coherence time T_2, by mitigating both static inhomogeneities and spin-spin interactions, beyond what is achievable with a single-pulse Hahn echo.

Compared to the Hahn echo 2.2.2, the CPMG sequence provides enhanced protection against both slow environmental noise and control imperfections. The repeated π pulses act as a dynamical filter, suppressing low-frequency noise and maintaining transverse coherence over longer durations. Moreover, by applying the $\pi/2$ and π pulses around orthogonal axes, the sequence compensates for consistent rotation errors that would otherwise accumulate [36]. This arrangement causes these pulse errors to cancel out in pairs, making the sequence more robust and stable over many cycles. Consequently, the measured T_2 with the CPMG method is typically longer than the T_2 obtained with the Hahn echo method ($T_{2,\mathrm{CPMG}} > T_{2,\mathrm{Hahn}}$). In addition to extending coherence, the CPMG sequence also provides the advantage of faster measurements.

Unlike Hahn echo measurements, where the system must be re-initialized for each delay τ, a single CPMG sequence yields multiple echoes from which T_2 can be extracted.

While the CPMG sequence significantly extends T_2, it is not without limitations. Although the sequence helps correct for systematic pulse errors, such as consistent over- or under-rotation by using orthogonal pulse axes, it is still sensitive to random pulse imperfections. Inaccuracies in pulse amplitudes, timing jitter, or phase noise can accumulate over multiple π pulses and reduce the effectiveness of refocusing. Additionally, applying too many pulses in quick succession can introduce heating effects or technical constraints that limit the achievable coherence time extension. As a result, there is a practical limit to how much T_2 can be improved using dynamical decoupling techniques [37].

Having concluded our discussion on the theoretical background of our system and the experimental techniques, we now proceed to describe our experimental setup.

3 Experimental Setup

In this chapter, we detail the experimental setup used to investigate the properties of our spin system. It consists of several key components essential for performing our measurements.

We begin by introducing the components of our hybrid system: sodium atoms, which serve as our spin ensemble and are embedded as impurities in a neon crystal at cryogenic temperatures, and the superconducting microwave cavity used to couple to this ensemble. We then describe the cryogenic setup used to cool the system to millikelvin temperatures, followed by the microwave setup responsible for generating, controlling, and detecting the microwave signals that interact with the spins.

3.1 Hybrid System

3.1.1 Sodium

Sodium (^{23}Na) was chosen as the spin system in our hybrid system due to its favorable properties for coupling to a microwave resonator. As an alkali atom with only one valence electron, it has a simple atomic structure and a ground-state hyperfine transition at about 1.77 GHz [38], which lies in the microwave range. This makes it well suited for magnetic coupling to our superconducting resonator (section 3.1.2). Compared to other alkali atoms like rubidium, sodium has a simpler hyperfine structure, it can also be introduced into the crystal quite easily by heating a sodium source during the matrix growth process (section 3.2.2). When embedded in solid neon, which is chemically inert and has no nuclear spin, the sodium atoms are well isolated from environmental noise and maintain their quantum properties. These features make sodium a strong candidate for studying coherent spin–resonator interactions and long spin coherence times.

The ground-state electronic configuration of sodium is

$$\text{Na: } 1S^2\,2S^2\,2P^6\,3S^1 = [\text{Ne}]\;3S^1$$

This single 3S valence electron defines the spin-$\frac{1}{2}$ system used in our experiment. A Bohr model of the sodium atom is shown in figure 3.1.

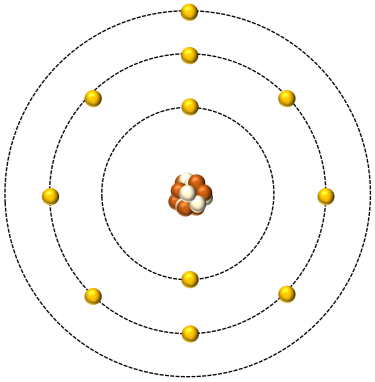

Figure 3.1: Bohr model of the sodium atom showing the electron configuration in the ground energy level.

The ground and first excited energy levels of sodium are shown in figure 3.2 below. The diagram illustrates both the ground state $3S$ as well as the excited state $3P$. The state $3P$ is further split into two different levels due to fine structure which is a result of coupling between the orbital angular momentum L of the electron in the outer shell and its spin angular momentum S. The total angular momentum J is given by:

$$|L - S| \leq J \leq L + S \tag{3.1}$$

For the ground state $3S$, where $L = 0$ and $S = 1/2$, the total angular momentum J is $1/2$, so that we only have one fine structure level $3S_{1/2}$. In the case of the excited state $3P$ however, we have $L = 1$ and $S = 1/2$ such that two different fine structure levels appear, $3P_{1/2}$ with $J = 1/2$ and $3P_{3/2}$, with $J = 3/2$ [38].

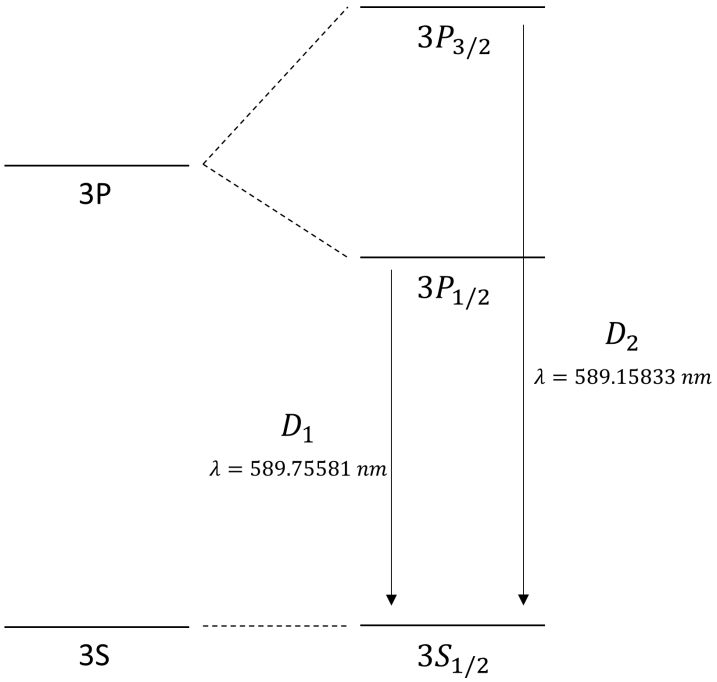

Figure 3.2: Energy level diagram of sodium, showing the fine structure splitting of the $3P$ state and the unsplit ground state $3S_{1/2}$. The D_1 and D_2 transitions between the $3S_{1/2}$ state and the $3P_{1/2}$ and $3P_{3/2}$ states, respectively, are also indicated. All other lower energy states are omitted for clarity.

In addition to fine structure, energy levels can undergo further splitting due to hyperfine interactions. This splitting arises from the interaction between the magnetic moment of the nucleus and the magnetic field generated by the orbiting electron. In sodium, the nucleus has a non-zero spin, which couples to the electron's total angular momentum J. This coupling results in additional energy shifts, further splitting the fine structure levels into hyperfine levels. The total angular momentum F is a combination of the nuclear spin I and the electronic total angular momentum J where the number of hyperfine levels depends on the values of I and J:

$$|J - I| \leq F \leq J + I \tag{3.2}$$

The sodium nuclear spin is $I = 3/2$ and for its ground state $3S_{1/2}$, we have $J = 1/2$, so we get $F = 1$ or $F = 2$. The resulting energy shifts are typically smaller than the fine structure splitting. A presentation of the hyperfine splitting of the sodium ground state $3S_{1/2}$ is given in figure 3.3.
When an external magnetic field is applied, the hyperfine levels of sodium experience further splitting due to the Zeeman effect [39]. In the absence of a magnetic field,

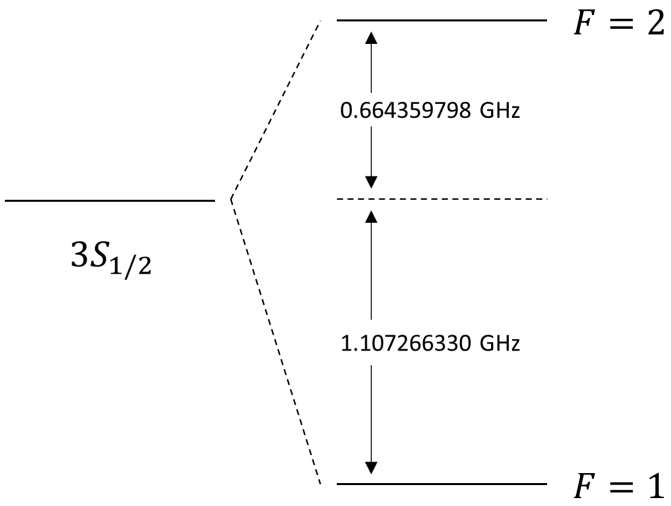

Figure 3.3: Hyperfine levels of the sodium ground state $3S_{1/2}$, showing the splitting into $F = 1$ and $F = 2$ levels.

the hyperfine levels are degenerate for a given total angular momentum F. However, when a magnetic field is introduced, each hyperfine level splits into $2F + 1$ sublevels corresponding to the different possible projections of the total angular momentum F along the direction of the magnetic field. These sublevels are characterized by the magnetic quantum number m_F, which ranges from $-F$ to $+F$ in integer steps. The energy shifts induced by the magnetic field are proportional to the magnetic field strength [40]:

$$\Delta E = \mu_B g_F m_F B_z \tag{3.3}$$

where B_z is the applied magnetic field, which, without loss of generality is taken to be along the the z-direction, μ_B the Bohr magneton and g_F the Landé g-factor for the total angular momentum F.

However, this formula only applies in the weak-field regime. For strong magnetic fields the interaction dominates the hyperfine energies and this is known as the Paschen-Back regime. In order to describe the splitting of the energy levels across a range of magnetic field strengths, including intermediate field strengths, the Breit-Rabi formula [38] is used:

$$E = -\frac{\Delta E_{HF}}{2(2I+1)} + g_I \mu_B m B_z \pm \frac{\Delta E_{HF}}{2}\sqrt{1 + \frac{4mx}{2I+1} + x^2} \tag{3.4}$$

where ΔE_{HF} is the hyperfine splitting at zero magnetic field. As can be seen in figure 3.3, this value for sodium is equal to 1.771 GHz [38]. Furthermore, x is given by the expression

$$x = \frac{(g_J - g_I)\mu_B B}{\Delta E_{HF}} \tag{3.5}$$

where g_J and g_I are the g-factors for the electron and the nucleus respectively. Equation (3.4) is used in figure 3.4 to show the splitting of the hyperfine levels of the sodium ground state $3S_{1/2}$ due to the presence of a magnetic field.

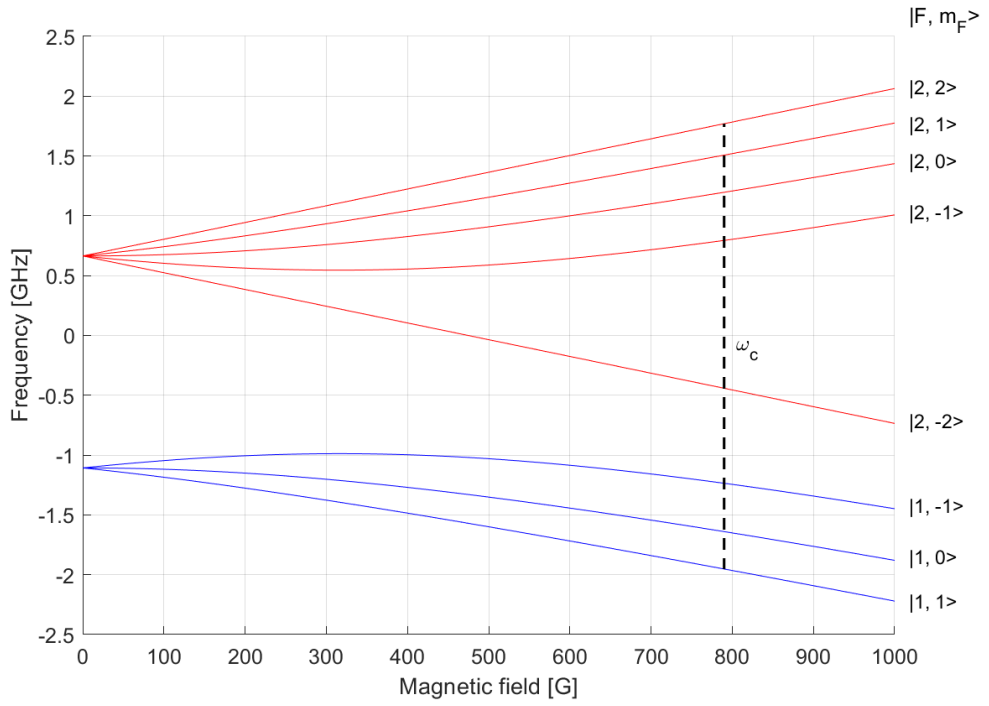

Figure 3.4: Energy level diagram showing the splitting of the hyperfine levels of the sodium ground state $3S_{1/2}$ as a function of an external magnetic field, calculated using the Breit-Rabi formula (3.4). The dashed line indicates the transition between the $|1, 1\rangle$ and $|2, 2\rangle$ levels, which we couple to our superconducting resonator. The resonator will be discussed in the next section 3.1.2.

With the magnetic field precisely tuned to match the energy difference between the hyperfine sublevels, we can achieve resonance conditions with the microwave cavity used in our experiment. This ability to vary the magnetic field allows us to selectively address and couple specific transitions between the hyperfine sublevels. As illustrated by the dashed line in figure 3.4, this particular transition is used for optimizing the interaction of our spin system with the microwave field. Achieving this resonance is essential for

probing the coherence properties of the sodium spins and conducting techniques, such as Hahn-echo and CPMG sequences, with which we measure coherence times T_2. In the next section, we will go into the details of the microwave cavity that enables this precise coupling and resonance, exploring how it integrates with our experimental setup.

3.1.2 Superconducting Resonator

The superconducting resonator is a crucial element in our experimental setup, enabling strong coupling between the sodium spin ensemble and the microwave field. It is fabricated on a 330 µm-thick sapphire substrate, with a 200 nm thick niobium (Nb) layer patterned in a spiral shape [41], as shown in figure 3.5. This spiral forms a planar LC circuit: the inductance L comes from the coiled spiral turns, similar to a flattened solenoid, generating a magnetic field extending out of the plane, while the capacitance C arises from the gaps between adjacent turns, where electric field lines build up across these small distances. Together, this LC circuit supports a sharp microwave resonance, with energy oscillating back and forth between the magnetic and electric fields. The resonance occurs at around 3.75 GHz in vacuum 3.6, and the magnetic field is significant up to about 120 µm above the plane [41], beyond which it decays. The superconducting nature of niobium minimizes resistive losses, enabling a high quality factor at cryogenic temperatures.

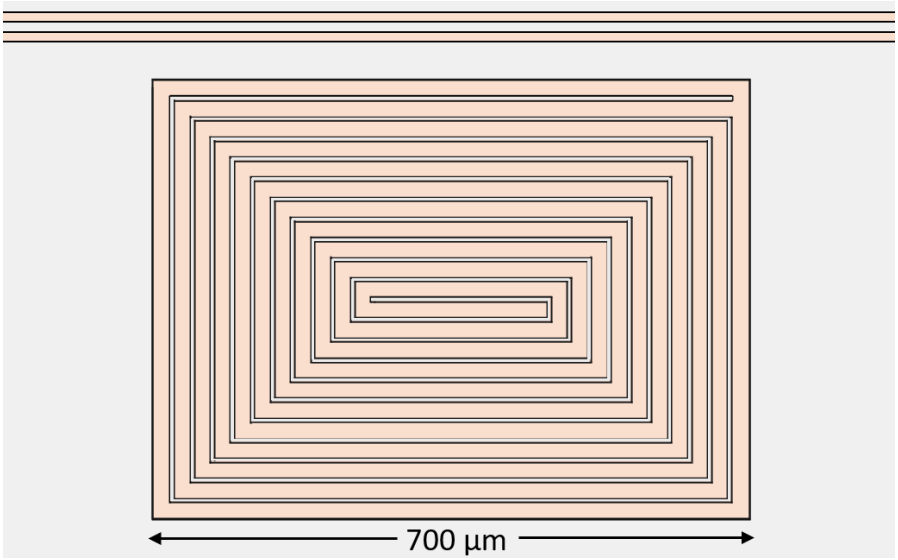

Figure 3.5: Schematic of the superconducting spiral resonator, patterned in a niobium (Nb) layer (gray) on a sapphire substrate (orange). The outer Nb area forms a ground plane. A coplanar waveguide (CPW) feedline, consisting of a central Nb strip separated from the ground plane by narrow gaps, delivers and detects the microwave signals. The feedline couples inductively to the spiral, as the magnetic field of the traveling wave in the CPW overlaps with the magnetic field oscillating in the resonator.

The transmission spectrum of the superconducting resonator provides key information about its resonance frequency and quality factor. In the measurement setup, microwave signals travel along the coplanar waveguide (CPW) feedline that passes above the spiral, as shown in figure 3.5. At the resonance frequency, part of the signal energy is coupled into the resonator, where it is temporarily stored but mostly dissipated. This loss leads to a characteristic dip in the transmitted signal measured along the feedline. The measurement is performed using a Vector Network Analyzer (VNA), which generates a continuous wave signal across a range of frequencies and measures the transmitted signal power, expressed as the $|S_{21}|^2$ parameter in dB. The resulting spectra are analyzed to extract the resonance frequency and quality factor.

The resonance feature in the transmission spectrum can be modelled using a Lorentzian function. However, to accurately extract the resonance frequency and quality factor from our measured transmission spectrum, we fit the data using a complex Fano lineshape [42, 43]. This model accounts for the interference between the discrete cavity mode and a weakly coupled background continuum, which leads to an asymmetric resonance profile as can be seen in figure 3.6. The expression used is:

$$S_{21}(f) = A \cdot \frac{i\kappa}{f - f_0 - i\kappa} + r\, e^{i\phi} \tag{3.6}$$

where f_0 is the cavity resonance frequency, κ is the half width at half maximum (HWHM) of the resonance, described also as the decay rate of the cavity field in the Maxwell-Bloch equations (2.73), A is the amplitude and $r\, e^{i\phi}$ represents the background signal interfering with the cavity response.

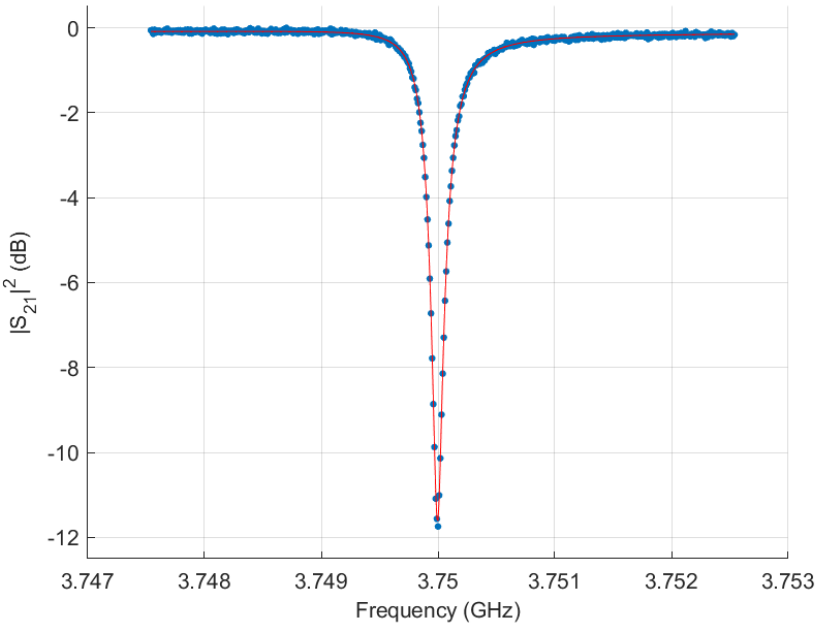

Figure 3.6: Transmission spectrum of the superconducting resonator in vacuum before crystal growth. The measured $|S_{21}|^2$ parameter (in dB) is shown in blue, with a Fano fit using equation (3.6) shown in red. From the fit, the resonance frequency and HWHM are extracted, which are then used to determine the resonator's quality factor.

The full transmission spectrum is obtained by taking the squared magnitude $|S_{21}(f)|^2$, which is then fitted with (3.6) and compared to the experimental data. The quality factor is then calculated as:

$$Q = \frac{f_0}{2\kappa} \tag{3.7}$$

In vacuum before crystal growth, the transmission spectrum shows a clear dip centered around 3.75 GHz, as illustrated in figure 3.6. The fit yields a center frequency of approximately 3.7499 GHz and a HWHM of 132.7 kHz, resulting in a quality factor Q of 14129.

After the sodium-neon crystal forms on the resonator surface (more on this process later in section 3.2.2), the transmission spectrum exhibits a shift in the resonance frequency as illustrated in figure 3.7. The addition of the neon matrix alters the dielectric constant around the resonator, lowering the resonance frequency to approximately 3.714 GHz. This behavior can be understood from the LC circuit analogy mentioned earlier: an increase in the relative permittivity (dielectric constant) of the environment increases the effective capacitance C, which according to $f_0 \propto 1/\sqrt{LC}$, leads to a decrease in the resonance frequency. Despite this shift, the HWHM remains largely unchanged, and the resulting quality factor Q stays high. The fit shows a center frequency shifted to 3.7137 GHz with a HWHM of 139.4 kHz, corresponding to a quality factor Q of 13320.

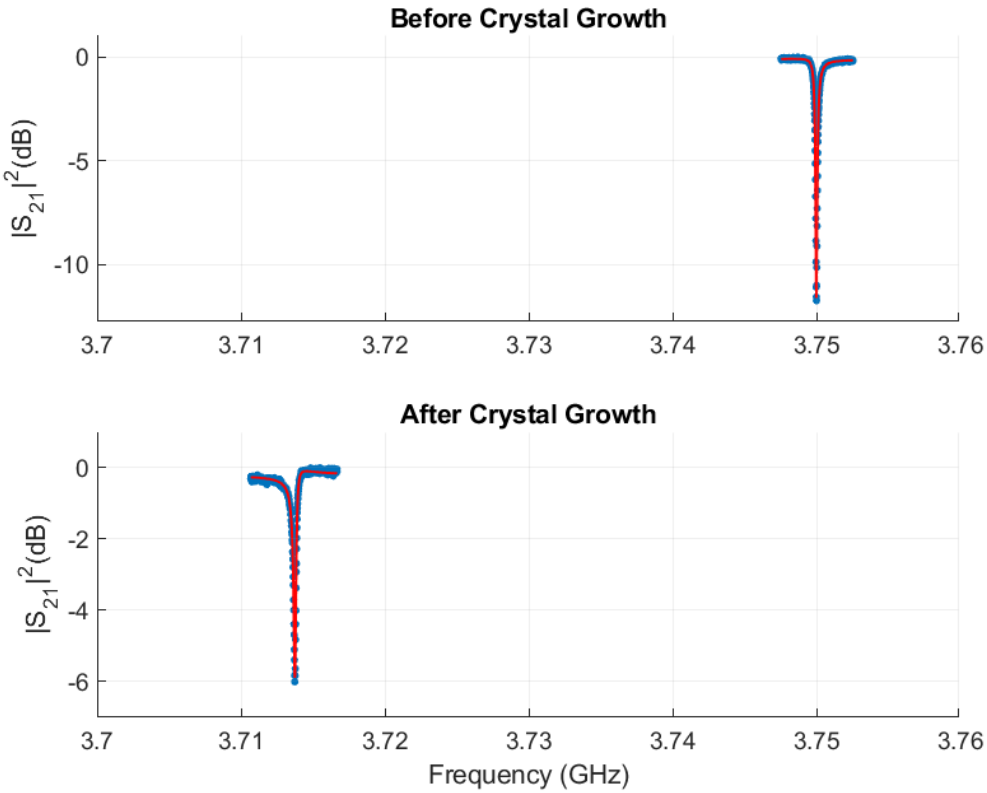

Figure 3.7: Transmission spectra of the superconducting resonator before (top) and after (bottom) crystal growth. The lower resonance frequency after crystal formation (~ 3.714 GHz) reflects the change in the dielectric environment caused by the sodium-neon matrix.

This shift in resonance frequency confirms the formation of the sodium-neon crystal and reflects the changes in the resonator's electromagnetic environment. Once the sodium-neon crystal is fully grown, the resonator can couple resonantly to the sodium spin ensemble. By carefully tuning an external magnetic field, we align the energy difference between the $|1,1\rangle$ and $|2,2\rangle$ hyperfine levels of sodium to match the shifted resonance frequency (see section 3.1.1 for details on sodium hyperfine levels). In our experiment, we use Helmholtz coils to apply a magnetic field, which we vary to shift the energy levels of the sodium atoms, until the energy difference corresponds to the resonance frequency of the superconducting resonator. Achieving this resonance condition is critical for strong coupling, which enhances the coherent exchange of energy between the microwave cavity and the spin system, leading to a collective response of the spin ensemble.

The collective nature of the coupling between the spin ensemble and the cavity is described by the Tavis-Cummings model, where the effective coupling strength $g_{\text{coll}} = \sqrt{N}g$ is enhanced by the number of participating spins N. Achieving such strong collective coupling is essential for observing coherent spin-resonator interactions and enables the implementation of techniques such as Hahn echo and CPMG sequences for

measuring coherence times.

Figure 3.8 provides an actual image of the resonator and surrounding Helmholtz coils used for magnetic field application within the ADR fridge.

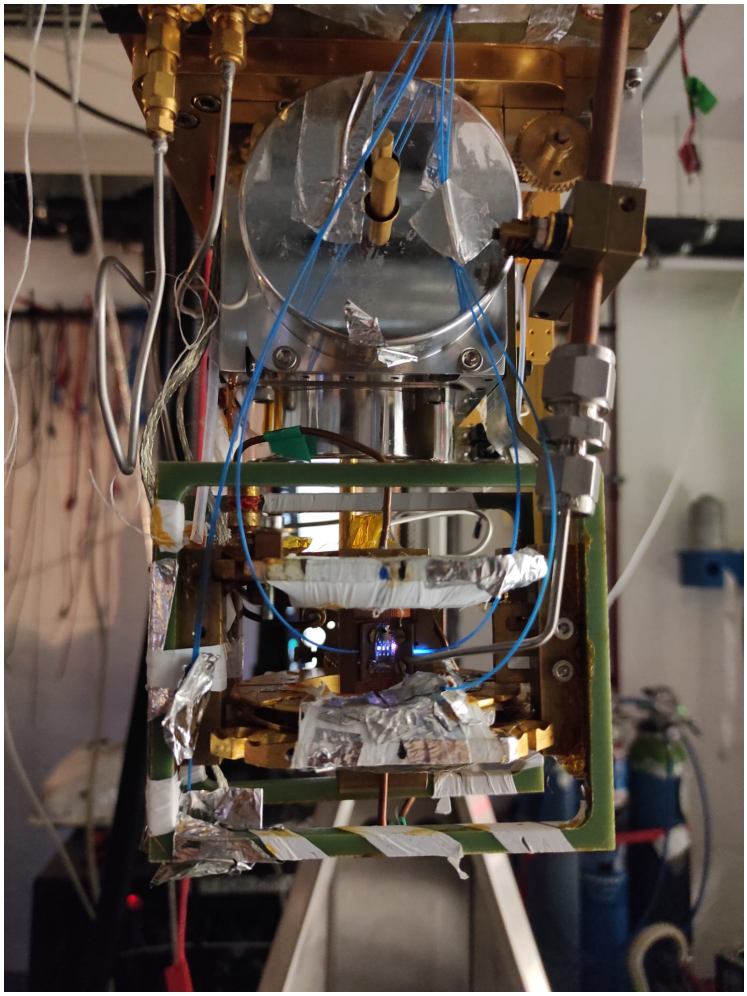

Figure 3.8: Overview of the experimental setup, showing the superconducting resonator positioned within the ADR fridge, with Helmholtz coils mounted around it to apply the magnetic field. The ADR fridge provides the low-temperature environment required for superconductivity and spin ensemble measurements (details in section 3.2).

3.2 Adiabatic Demagnetization Refrigerator (ADR)

A cryostat is a device that enables experiments to be carried out at very low temperatures by minimizing thermal noise and stabilizing the system. In our experiment, the cryostat is based on an Adiabatic Demagnetization Refrigerator (ADR), which achieves millikelvin temperatures by leveraging the magnetocaloric effect in a paramagnetic salt. The ADR used in our setup is a commercial system from STARCRYO [44], designed

to reach millikelvin temperatures and equipped with microwave feedlines and measurement ports for our experiments. This ultra-low temperature environment reduces the thermal photon occupation in the cavity and ensures that the sodium spins relax into their ground state, providing the ideal starting point for precision measurements (see Chapter 4). Furthermore, operating at low temperatures allows the use of superconducting resonators, such as the one discussed in 3.1.2, which have higher quality factors Q, which correspond to lower damping rates. For a detailed technical description of the ADR system and its implementation, see [45, 46].

3.2.1 Operation Principle

The ADR's cooling cycle is based on aligning and then randomizing the magnetic moments of a paramagnetic salt. It proceeds in three main stages:

- Initial Magnetization: A current is applied to a superconducting magnet surrounding the salt, generating a strong magnetic field (up to $\sim$ 4T). While the paramagnetic salt is thermally connected to the $\sim$ 3K cooling stage (often referred to as the cold bath) via a heat switch, this field aligns the magnetic moments of the salt and brings it into thermal equilibrium with the bath.

- Adiabatic Demagnetization: The heat switch is opened, thermally isolating the salt from the bath. The magnetic field is then slowly reduced in an adiabatic process, during which the previously aligned magnetic moments begin to randomize. As this disordering increases the entropy of the spin system, the energy required to maintain constant entropy is drawn from the internal energy of the coldest stage. This results in a drop in temperature of both the paramagnetic salt and the surrounding components, including the copper box housing the resonator and spin ensemble, reaching the millikelvin regime. Because this process occurs without heat exchange with the environment, the system can reach these very low temperatures stably.

- Thermal Stabilization: Once the target temperature is reached, the ADR can maintain it for several hours. Although the current in the superconducting magnet is fixed during this period, small heat leaks inevitably warm the system slowly. When the temperature eventually rises to about $\sim$ 2.7K, the ADR must be recycled: the heat switch is closed again to re-establish contact with the $\sim$ 3K bath, the salt is re-magnetized by applying a strong current, and a new adiabatic demagnetization is performed. This cyclical process of magnetization and demagnetization sets the operational time window for low-temperature experiments.

The ADR setup also includes nested thermal shields at the 300 K, 50 K, and 3 K stages, minimizing heat transfer to the coldest stage. These shields have aligned holes to allow sodium atoms from the atomic impurities oven to reach the resonator surface (see section 3.2.2). Integrated optical and microwave spectroscopy tools further enable precise monitoring and characterization of the sodium spin ensemble. The overall configuration can be seen in figure 3.9.

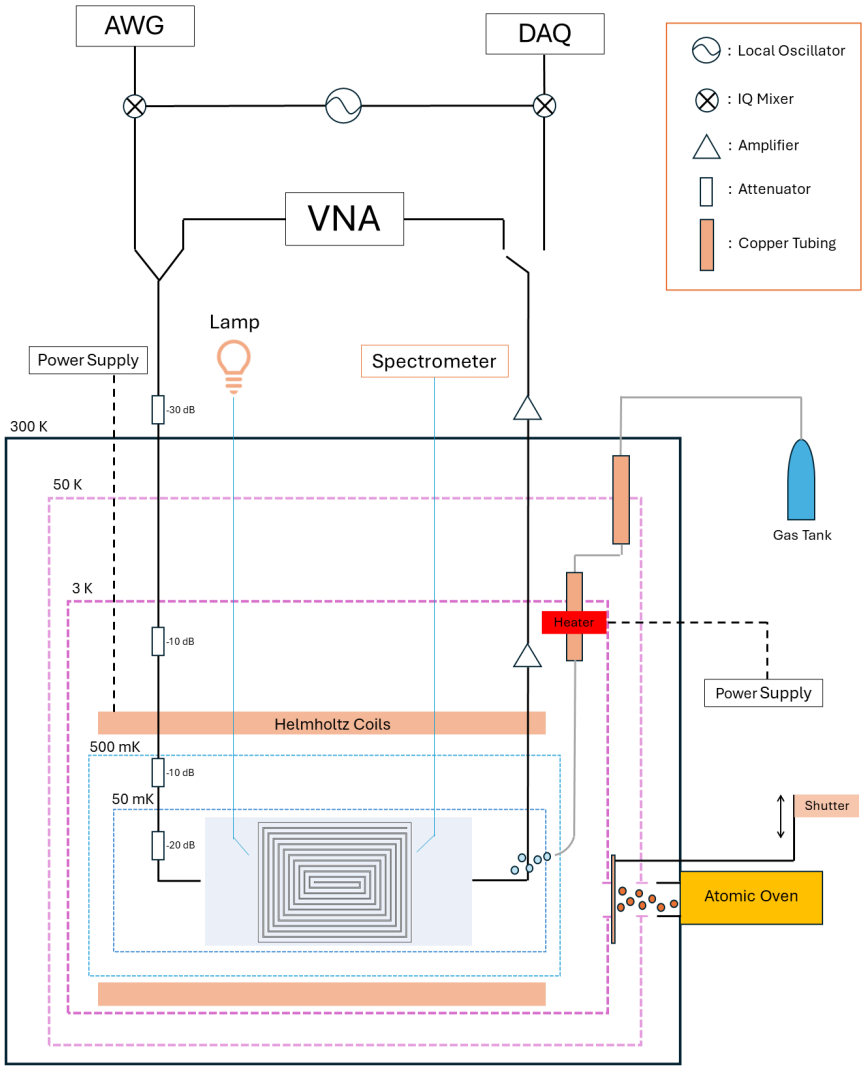

Figure 3.9: Schematic of the ADR cryogenic setup used for crystal growth and spin ensemble measurements. The system features nested thermal shields to minimize heat transfer and aligned holes for sodium atom deposition onto the resonator. The microwave measurement setup 3.3 includes an input (down) line delivering pulses from the Arbitrary Waveform Generator (AWG) and a Vector Network Analyzer (VNA) for frequency-domain characterization. The output line collects signals from the resonator, which are amplified by low noise amplifiers before digitization (DIG). A microwave switch on the output line enables toggling between steady-state frequency-domain measurements (VNA) and time-resolved measurements. Integrated optical access enables optical bleaching and spectroscopic analysis of the sodium-neon crystal 3.2.2.

The photograph on figure 3.10 illustrates the external structure of the ADR as used in our experiment.

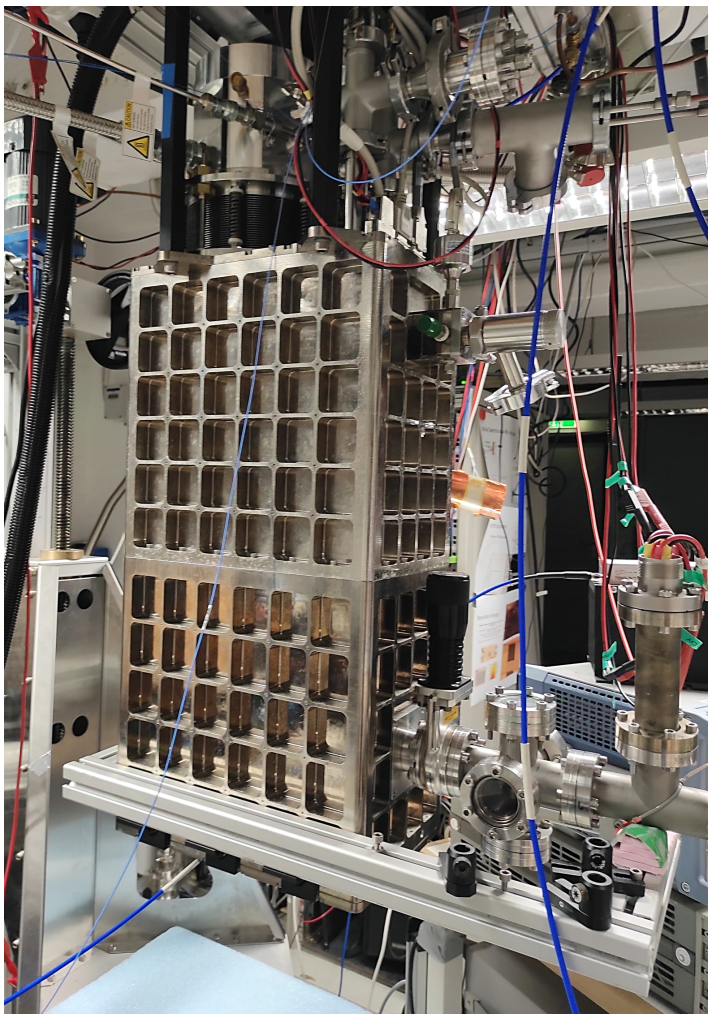

Figure 3.10: Photograph of the ADR system in operation, showing its external structure and connection ports for experiments.

With the ADR achieving these low temperatures, the next step is the controlled formation of the sodium-neon crystal.

3.2.2 Crystal Growth

Our cryogenic system enables the controlled growth of a neon crystal with sodium atoms embedded as impurities on the surface of the resonator [46], located at the coldest stage of the ADR. This millikelvin environment is essential for forming the spin ensemble that interacts with the superconducting resonator.

To initiate crystal growth, neon gas and sodium atoms are introduced separately into the ADR sample chamber at cryogenic temperatures. The neon gas, serving as the host matrix, is directed onto the resonator surface, where it condenses to form a

crystalline structure. The gas travels through the cryosystem via a series of stainless steel and copper tubes that cool the gas from room temperature to slightly above the boiling point ($\sim 27\,\mathrm{K}$). After the gas exits the tube at the final cooling stage, it begins condensing on top of the superconducting resonator. Simultaneously, sodium atoms emitted from the nozzle of the sodium oven travel directly through aligned openings in the thermal shields and get embedded as impurities within the forming neon matrix. To create atomic Na, an atomic beam oven is heated to $\sim 170\,^{\circ}\mathrm{C}$ in a separate chamber directly attached to the outer vacuum shield. Na atoms reach the resonator through the holes in the 50K and the 3K shield as was shown in figure 3.9. The process of directing the host matrix gas and impurities toward the resonator is shown in figure 3.11, illustrating the deposition of these gases onto the resonator to initiate crystal formation.

The ADR's precise temperature control during the crystal growth phase is important because a stable environment ensures consistent growth conditions. Additionally, the process can be monitored in real-time by tracking shifts in the resonator's resonance frequency, as introduced in section 3.1.2. These resonance shifts occur due to changes in the dielectric environment around the resonator as the crystal forms and provide a way to monitor the growth and estimate the thickness of the neon matrix.

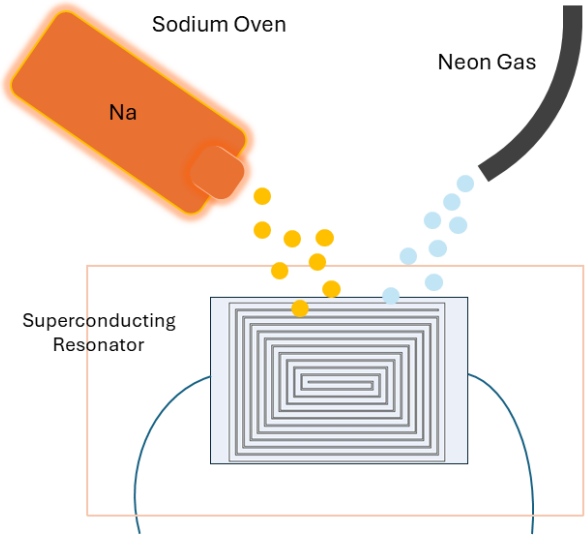

Figure 3.11: Illustration of the crystal growth process within the ADR setup, showing the superconducting resonator as neon gas (host matrix) and sodium impurities are directed onto its surface. The ADR fridge enables stable crystal growth.

As mentioned in section 3.1.2, Helmholtz coils are used to generate a uniform magnetic field across the resonator, allowing us to tune the energy levels of the sodium

spin ensemble into resonance with the microwave field of the resonator. An illustration of the resonator with the sodium-neon matrix formed on its surface, surrounded by Helmholtz coils for magnetic field application, and connected to a Vector Network Analyzer (VNA) for steady-state transmission measurements is shown in figure 3.12. To establish the precise resonance condition for our experiment, a magnetic field scan was conducted, systematically varying the magnetic field until the frequency of the $|1,1\rangle$ to $|2,2\rangle$ transition, matches the resonator frequency. The results of this resonance alignment, including the observed Rabi splitting, will be detailed in the Results Chapter 4.

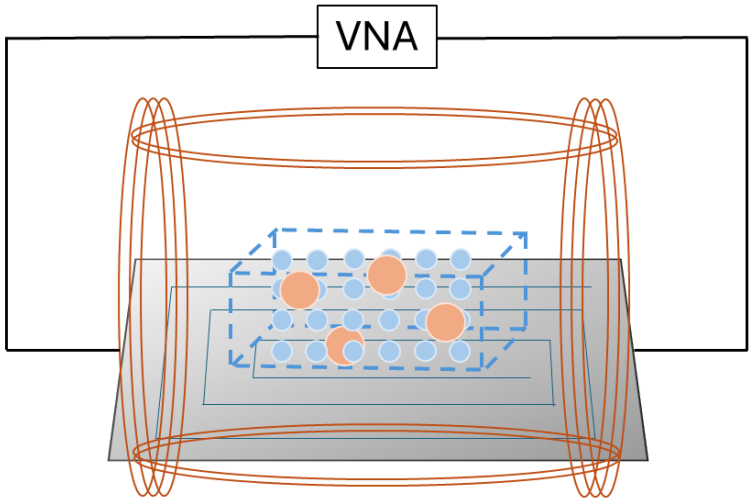

Figure 3.12: Illustration of the experimental setup, showing the superconducting resonator with the sodium spin ensemble on top (represented as spherical elements) and Helmholtz coils used for magnetic field application. The setup is connected to a Vector Network Analyzer (VNA) for transmission spectrum measurements.

To optimize the properties of the sodium-neon spin ensemble, we perform optical bleaching inside the ADR system. Optical bleaching has been empirically shown to enhance the observed coupling strength in hybrid quantum systems [47, 48]. Although the exact physical mechanism remains uncertain, it is believed that the illumination supplies localized energy that allows sodium atoms to transition from less favorable positions in the crystal, where coupling to the microwave field is weak, into sites where stronger coherent coupling can occur [46]. This realignment may increase the number of effectively coupled spins in the ensemble. In our experiment, bleaching light consists of a broad white-light spectrum, generated by two LEDs—one centered at 447 nm (blue) and one at 517 nm (green)—along with a tungsten lamp. These light sources are coupled into an optical fiber that enters the cryostat and illuminates the sodium-neon

crystal at a 45° angle to the resonator substrate. We consistently observe a stronger coupling 4.1 only after bleaching has been applied. However, the underlying physical process is still the subject of ongoing research, and no definitive explanation currently exists.

With the ADR system providing a controlled environment for crystal growth and precise magnetic field tuning, the next section will focus on the microwave setup, which is essential for performing time-resolved measurements and studying the dynamic properties of the newly formed spin ensemble.

3.3 Microwave Setup

3.3.1 Overview of the Microwave Setup

The microwave setup in our experiment is critical for generating, transmitting, and detecting microwave signals that probe the sodium spin ensemble. Working together with the ADR system, it enables both steady-state and time-resolved measurements with high precision. Microwave signals are transmitted to the resonator through coaxial cables, which are thermally anchored at multiple stages of the ADR to reduce heat transfer. The setup also incorporates essential components such as attenuators and amplifiers to ensure that the signals remain within the desired power and frequency ranges during transmission and detection [49].

As already mentioned before, for the steady-state measurements, a Vector Network Analyzer (VNA) is used to sweep the input microwave frequency and analyze the transmission spectrum of the resonator. This allows for precise determination of the resonance frequency and quality factor, as described in section 3.1.2. For time-resolved experiments, the microwave setup utilizes an Arbitrary Waveform Generator (AWG) to generate precise pulse sequences, enabling measurement techniques such as Hahn echo or CPMG measurements. Detection of the spin ensemble's response is achieved using demodulation techniques, which will be detailed in the following sections.

Overall, the microwave setup provides the necessary flexibility and precision to explore both the steady-state and dynamic properties of the sodium spin ensemble. Figure 3.13 presents a schematic overview of the key components involved in the time-resolved measurement setup. The local oscillator (LO) provides a continuous microwave carrier signal that feeds two IQ mixers. The first mixer combines the LO with the baseband I and Q signals generated by the AWG to produce the modulated microwave pulse (P_{IN}) sent to the resonator. After interaction with our sodium spin ensemble, the outgoing microwave signal (P_{OUT}) is amplified and demodulated by the second

IQ mixer, which uses the same LO as reference to extract the returning I' and Q' quadrature components. These are digitized and recorded by the DAQ card for analysis. Section 3.3.3 explains the IQ mixing technique and the mathematical framework behind the modulation/demodulation process.

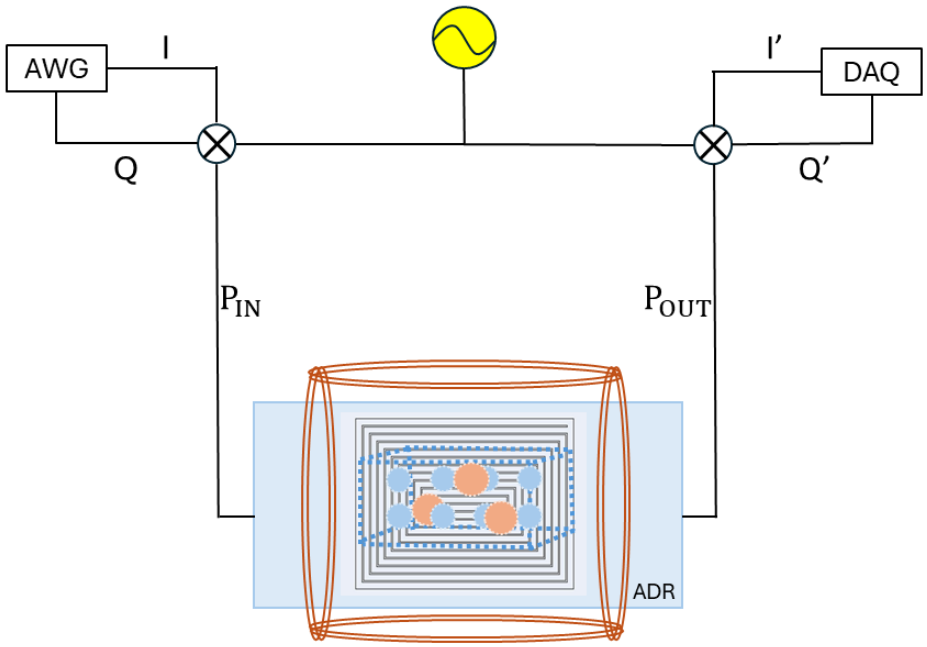

Figure 3.13: Schematic of the microwave setup showing the local oscillator (LO), the two IQ mixers used for upconversion and downconversion, the AWG generating the baseband I and Q signals, and the data acquisition (DAQ) card recording the demodulated I' and Q' signals after interaction with the hybrid system.

3.3.2 Signal Generation, Transmission and Detection

The generation and transmission of microwave signals to the superconducting resonator are central to the experiment, enabling precise manipulation and control of the sodium spin ensemble. This setup relies on specific components to ensure signal stability and minimal thermal noise.

Microwave signals are generated using two primary sources: the Vector Network Analyzer (VNA) and the Arbitrary Waveform Generator (AWG). For steady-state measurements, the VNA produces a continuous wave (CW) signal that is swept across a range of frequencies to measure the transmission spectrum of the resonator, like the one discussed in section 3.1.2. This enables precise determination of the resonance

frequency and quality factor of the resonator-spin system. For time-resolved measurements, the AWG generates the baseband waveforms for the I and Q quadrature components, which define the pulse sequences required for experiments such as Hahn echo and CPMG protocols. These waveforms are then upconverted onto the microwave carrier frequency by the IQ mixer.

The carrier signal, typically set to the cavity's resonance frequency (≈ 3.714 GHz) and generated by a continuous wave microwave source, referred to as local oscillator (LO), is mixed with these two quadrature components using an IQ mixer. The mathematical details of this IQ mixing procedure, including how the I and Q components modulate the carrier signal, will be described in the next section 3.3.3. The resulting signal is then amplified and transmitted to the resonator.

The transmission line also contains the following key components: attenuators, which are placed along the transmission line to reduce the power of the microwave signals and prevent saturation of the resonator and sodium spin ensemble, and low-noise amplifiers, which are installed on the return path, to boost the weak signals emitted from the resonator, thereby improving the signal-to-noise ratio during detection.

After exiting the resonator, the amplified microwave signal is routed through coaxial cables to a data acquisition (DAQ) card integrated into a computer system. Using the reference signal from the local oscillator, the outgoing microwave signal can be decomposed back into I' and Q' components, which are then recorded and saved by the DAQ card for further analysis.

3.3.3 IQ Mixing

The IQ mixing technique plays a central role in our microwave setup, enabling precise control over the microwave signals interacting with the sodium spin ensemble. While the cavity resonance frequency lies in the GHz range (~ 3.714 GHz), the relevant dynamics, such as spin-cavity coupling or coherence decay, occur on much slower timescales, typically in the MHz range. By using IQ mixing, we effectively shift our signals into the rotating frame of the cavity, allowing us to modulate and detect microwave pulses at baseband (MHz frequencies). This not only simplifies the control of pulse shapes and sequences, but also reduces hardware requirements, enabling the use of slower, more accessible electronics for signal generation and detection.

Signal Modulation

Before entering the ADR system, the microwave signal is modulated using an IQ mixer. A carrier signal ω_p, typically tuned to the resonance frequency of the cavity ($\omega_\mathrm{p} \approx \omega_\mathrm{c} = 3.714$ GHz), is generated by a Local Oscillator (LO). This carrier signal is then

mixed with two quadrature components, the in-phase $I(t)$ and quadrature $Q(t)$ signals, generated by an Arbitrary Waveform Generator (AWG).

The mathematical representation of the modulated signal can be expressed as [23, 49]:

$$S(t) = I(t)\cos(\omega_{\mathrm{p}}t) - Q(t)\sin(\omega_{\mathrm{p}}t) \tag{3.8}$$

where $I(t)$ and $Q(t)$ are the time-dependent quadrature components of the waveform generated by the AWG, controlling the amplitude and phase of the microwave signal. This modulated signal is amplified and transmitted into the ADR system via coaxial cables, as described in section 3.3.2. The modulation process allows for the creation of complex pulse sequences required for time-resolved experiments such as Hahn echo and CPMG protocols.

Signal Demodulation

After interacting with the sodium spin ensemble within the resonator, the microwave signal exits the ADR system and undergoes demodulation to extract the new I' and Q' components. The signal is amplified using low-noise amplifier (LNA) and routed to the IQ mixer for demodulation.

The demodulation process uses the same LO signal that was employed for modulation, the outgoing signal is mixed with the LO signal, yielding two outputs:

$$\begin{aligned} I_{\mathrm{out}}(t) &= S'(t)\cos(\omega_{\mathrm{p}}t) \\ Q_{\mathrm{out}}(t) &= -S'(t)\sin(\omega_{\mathrm{p}}t) \end{aligned} \tag{3.9}$$

where $S'(t)$ is the modified signal coming out of the fridge.

Using trigonometric equations, these become

$$\begin{aligned} I_{\mathrm{out}}(t) &= \frac{I'(t)}{2}(\cos(2\omega_{\mathrm{p}}t) + 1) - \frac{Q'(t)}{2}\sin(2\omega_p t) \\ Q_{\mathrm{out}}(t) &= -\frac{I'(t)}{2}\sin(2\omega_p t) + \frac{Q'(t)}{2}(1 - \cos(2\omega_{\mathrm{p}}t)) \end{aligned} \tag{3.10}$$

These equations represent the demodulation process used to recover the in-phase and quadrature components of the outgoing signal. To extract $I'(t)$ and $Q'(t)$ of the signal after its interaction with the spin ensemble, the signal $S'(t)$ is multiplied (mixed) with reference signals $\cos(\omega_{\mathrm{p}}t)$ and $-\sin(\omega_{\mathrm{p}}t)$ followed by low-pass filtering. This procedure effectively removes the carrier frequency and isolates the slowly varying components that encode the amplitude and phase of the signal. Mathematically, this works because the multiplication generates a combination of high- and low-frequency terms, and by filtering out the fast oscillating parts, only the desired quadrature components remain.

These quadrature components are mathematically equivalent to the real and imaginary parts of the drive term in the driven Tavis-Cummings Hamiltonian (2.70). This correspondence arises because we work in the rotating frame of the cavity. Doing the same derivation as for the driven Tavis-Cummings Hamiltonian, gives:

$$\hat{H} = \hbar\Delta_c \hat{a}^\dagger \hat{a} + \frac{1}{2}\sum_{i=1}^{N} \hbar\Delta_s^i \hat{\sigma}_z^i + \sum_{i=1}^{N} \hbar g_i \left(\hat{\sigma}_+^i \hat{a} + \hat{\sigma}_-^i \hat{a}^\dagger\right) + \mathrm{i}\hbar I(t)\left(\hat{a}^\dagger - \hat{a}\right) + \hbar Q(t)\left(\hat{a}^\dagger + \hat{a}\right) \tag{3.11}$$

which leads to the modified first Maxwell-Bloch equation (the other two remain unchanged)

$$\langle \dot{\hat{a}} \rangle = -i\Delta_c \langle \hat{a} \rangle + \sum_j g_j \langle \hat{\sigma}_-^j \rangle + I(t) - iQ(t) - \kappa \langle \hat{a} \rangle \tag{3.12}$$

By comparing equation (3.12) to the first Maxwell-Bloch equation (2.73) from section 2.1.5, we can see that the two quadratures correspond to the real and imaginary part of the drive:

$$\eta = I(t) - \mathrm{i}Q(t) \tag{3.13}$$

Here, η represents the complex amplitude of the microwave drive field applied to the resonator. This field couples to the cavity and mediates the interaction with the spin ensemble, as described by the driven Tavis-Cummings Hamiltonian in Chapter 2.

The microwave setup outlined in this chapter allows precise probing of the sodium spin ensemble. By using IQ mixing the system enables accurate control and measurement of the spin dynamics. Together with the ADR environment, this setup forms the basis of our experimental measurements. The next chapter will detail the experimental techniques and present the results obtained with this setup.

4 Results

This chapter presents the main experimental results of this work. We begin by demonstrating strong coupling between the sodium spin ensemble and the superconducting resonator through a magnetic field scan and steady-state transmission measurements. We then turn to time-domain experiments, where we extract the coherence time T_2 using the Hahn echo and CPMG dynamic decoupling sequences.

4.1 Strong Coupling

An important requirement for these experiments is preparing the spin ensemble in a well-defined state. This is achieved by cooling the system to millikelvin temperatures using the ADR cryostat (see section 3.2.1), which enables the thermal initialization of the spins. At millikelvin temperatures, the sodium atoms embedded in the solid neon matrix are thermally polarized into the lower hyperfine level $F = 1$. The upper hyperfine level $F = 2$, which lies 1.771 GHz above $F = 1$ (see figure 3.3), becomes significantly less populated at these temperatures due to thermal suppression. This behavior is well described by Boltzmann statistics [50, 51], which predict that at high temperatures the population is distributed according to the degeneracy of each hyperfine level, while at low temperatures it concentrates overwhelmingly in the lower-energy manifold. Specifically, a plot of the population ratio for our sodium spin ensemble as a function of temperature is shown in figure 4.1, illustrating the transition from a thermal mixture to near-complete polarization at lower temperatures. At our operating temperature of 50 mK, indicated by a dashed line in the figure, approximately 77% of the atoms are thermally populated in the $F = 1$ manifold, based on the numerical calculation. This high degree of thermal polarization is one of the main reasons for working at millikelvin temperatures, as it ensures that the ensemble is initialized in a well-defined spin state and maximizes the number of atoms available for coherent coupling to our microwave resonator.

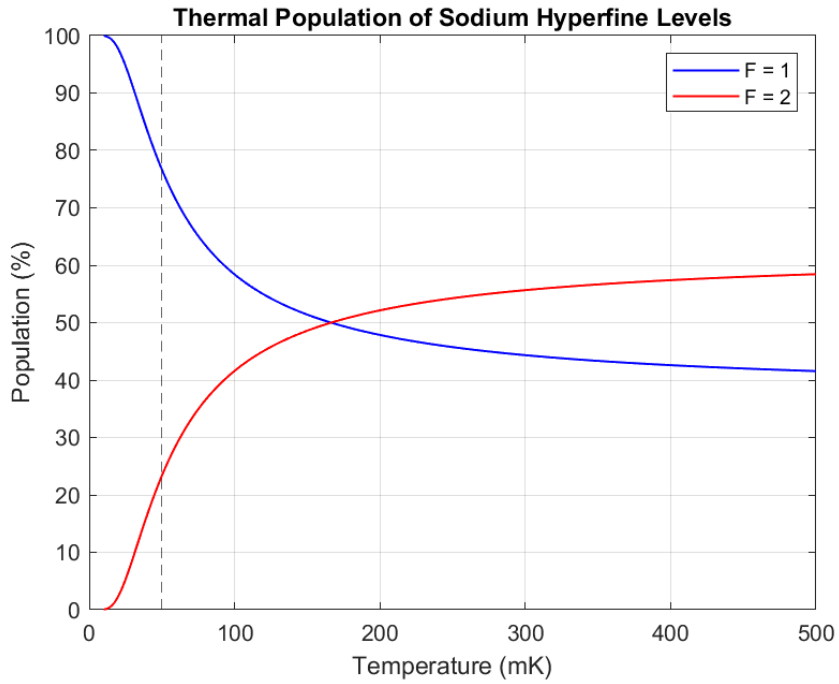

Figure 4.1: Thermal population distribution between the sodium ground-state hyperfine levels $F = 1$ and $F = 2$, calculated using Boltzmann statistics. At high temperatures, the populations reflect statistical weights (3:5), while at millikelvin temperatures the system is almost fully polarized into the $F = 1$ manifold. A vertical dashed line marks the operating temperature of 50 mK, where approximately 77% of the ensemble occupies the $F = 1$ manifold.

To address a specific hyperfine transition, we applied a tunable magnetic field using a pair of Helmholtz coils mounted inside our cryostat, as described earlier in section 3.1.2. The Zeeman effect lifts the degeneracy of the m_F sublevels, resulting in eight distinct energy levels $|F, m_F\rangle$. This splitting is accurately described by the Breit–Rabi formula (3.4), which provides the energy shifts of the Zeeman sublevels as a function of magnetic field. Using this expression, the energy deviations of all $|F, m_F\rangle$ magnetic substates from their zero-field values were calculated, corresponding to a transition tuned from the zero-field hyperfine splitting (1.771 GHz) to the resonator's frequency (3.714 GHz). These energy levels were then used to recompute the thermal population distribution at 50 mK using Boltzmann statistics, now accounting for the Zeeman-resolved structure. The result yields a combined population of approximately 88% in the $F = 1$ manifold, with the most populated state being $|1, +1\rangle$, which holds about 38% of the total ensemble. By tuning the magnetic field appropriately, we bring the $|1, +1\rangle \rightarrow |2, +2\rangle$ transition into resonance with the microwave cavity (see figure 3.4), thereby realizing an effective two-level system.

To demonstrate strong coupling between our sodium spin ensemble and the superconducting resonator, a magnetic field scan was performed around the resonator's resonance frequency. After the crystal was optically bleached, as described in sec-

tion 3.2.2, the magnetic field was swept over a range of approximately 780–800 G, and at each field value, the transmission spectrum $|S_{21}|^2$ was recorded using a Vector Network Analyzer (VNA). The data was stored as complex frequency-domain traces, which were subsequently processed by computing the squared magnitude of the complex transmission coefficient and converting the power to decibels. The result is shown in figure 4.2, where the vertical axis corresponds to the probe frequency of the VNA, the horizontal axis to the applied magnetic field, and the color scale to the normalized transmission power in dB. By tuning the external magnetic field appropriately, the spin ensemble is brought into resonance with the cavity, resulting in a spectrum that qualitatively matches the theoretical prediction in figure 2.6. The splitting observed at the intersection of the spin transition and cavity frequency corresponds to vacuum Rabi splitting, indicative of strong coupling between the resonator and the sodium spin ensemble.

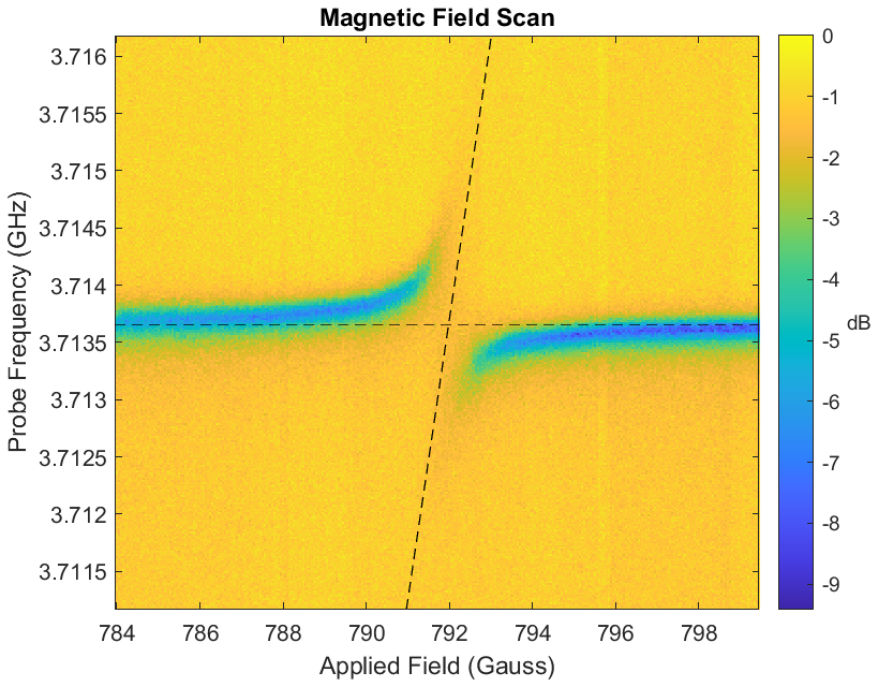

Figure 4.2: Transmission spectrum $|S_{21}|^2$ as a function of applied magnetic field and probe frequency, measured at 50 mK. The avoided crossing around $B = 792$ G and the cavity's frequency $\omega_c/2\pi = 3.7137$ GHz is characteristic of vacuum Rabi splitting, indicating strong coupling between the resonator and the sodium spin ensemble. The horizontal dashed line marks the bare cavity resonance, while the diagonal dashed line indicates the atomic transition frequency.

To quantitatively analyze the coupling strength, a vertical slice of the 2D magnetic field scan at a fixed magnetic field value near the avoided crossing was selected, specifically at $B = 792$ G. This yields a transmission spectrum as a function of probe frequency, shown in figure 4.3. The emergence of two distinct dips reflects the hybridization of the cavity mode and the collective spin excitation, forming polariton branches as

predicted by the Tavis–Cummings model which was discussed earlier 2.1.4. This spectrum was fitted using the steady-state solution to the Maxwell–Bloch equations (2.76), discussed in section 2.1.5, which describes the transmission of a cavity coupled to an inhomogeneously broadened spin ensemble.

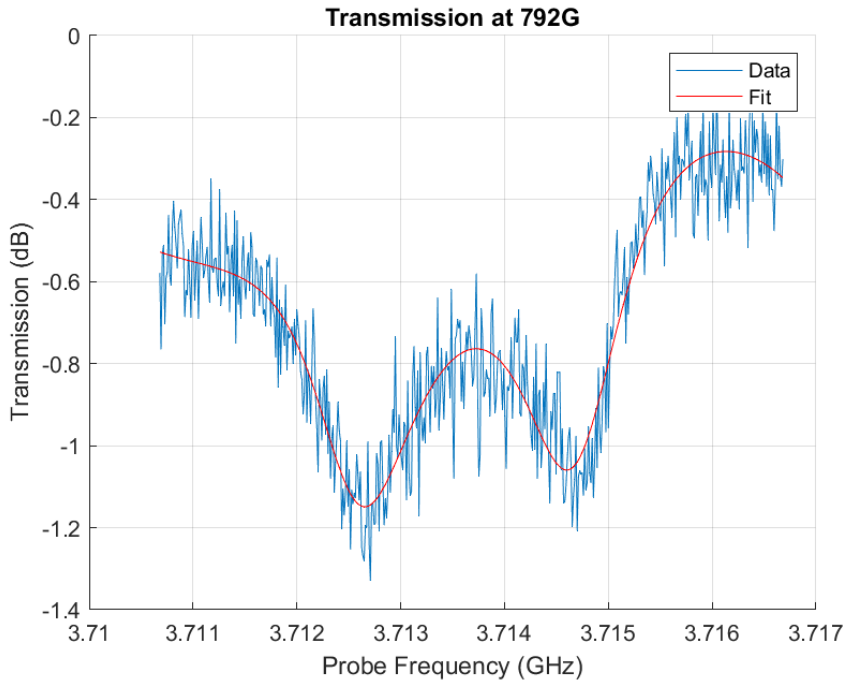

Figure 4.3: Transmission spectrum at a fixed magnetic field $B = 792\,\mathrm{G}$, as a function of probe frequency near the cavity resonance. The solid red line represents a fit using the steady-state solution of the Maxwell–Bloch equations (2.76). Extracted parameters are the collective coupling strength $g_{\mathrm{coll}}/(2\pi) = 0.96\,\mathrm{MHz}$, the spin distribution FWHM $\gamma_q/(2\pi) \approx 1.97\,\mathrm{MHz}$ and the q-parameter $q \approx 1$.

In the fit, several parameters were treated as free variables, including the collective coupling strength g_{coll} and ensemble linewidth γ_q (2.74), while keeping other parameters fixed based on prior measurements. The extracted spin distribution features a full width at half maximum (FWHM) of approximately 1.97 MHz and a q-parameter close to unity, indicating that the spin frequency distribution is nearly Gaussian. This result is consistent with previous independent measurements of the sodium spin ensemble's spin distribution done in our group. The fit also yielded a collective coupling strength of $g_{\mathrm{coll}}/(2\pi) = 0.96$ MHz. The cavity linewidth was fixed to $\kappa/(2\pi) = 140$ kHz, as it was independently extracted from the fit to the transmission spectrum of the resonator (see section 3.1.2). The transverse relaxation rate was fixed to $\gamma_\perp = 1/T_2$, using the value for T_2 obtained from the measurements presented later in this chapter (see section 4.2.1). The longitudinal relaxation rate $\gamma_\parallel = 1/T_1$ was set to zero in the fit. This is justified by previous measurements performed in our group, which found $T_1 \approx 8$ minutes, making the influence of T_1 processes negligible on the timescales relevant to our experiments.

Using the extracted parameters, we compute the cooperativity as

$$C = \frac{g_{\text{coll}}^2}{\kappa\Gamma} \approx 9.8$$

where Γ is the effective ensemble linewidth, which accounts for both the inhomogeneous broadening (FWHM of the spin distribution γ_q) and the individual spin dephasing $\gamma_\perp$ using equation (2.75). Since $C > 1$, the system is in the strong coupling regime, enabling time-resolved measurements of our spin ensemble's coherence presented in the following sections.

4.2 Coherence Measurements

4.2.1 Hahn Echo

To characterize the coherence time T_2 of our sodium spin ensemble, Hahn echo experiments were performed, following the pulse sequence introduced in section 2.2.2. As described earlier, the sequence consists of a $\pi/2$ pulse sent into our system, followed by a delay time τ and a stronger refocusing π pulse, after which the spin echo is detected via the emitted signal from the resonator after a second delay time τ.

In our experiment, rectangular microwave pulses were generated using the arbitrary waveform generator (AWG) as described in section 3.3. A key experimental challenge was identifying optimal values for the pulse amplitude and duration, particularly for the $\pi/2$ and π pulses. Initially, we applied a basic sequence ($\pi/2-\tau-\pi$) and monitored the resonator output in the time domain in search of an echo signal. The strategy that led to successful echo detection was to fix the π pulse to a specific duration $1\,\mu$s and calibrate its amplitude using the AWG, by tuning the output voltage until a clear echo signal was observed in the time-domain response of the resonator. With the π pulse set, we then systematically scanned both the amplitude and duration of the $\pi/2$ pulse to identify the settings that produced the largest spin echo. The resulting echo signals for several values of the delay time τ are shown in figure 4.4, clearly revealing the formation of spin echoes at times 2τ after the initial $\pi/2$ pulse.

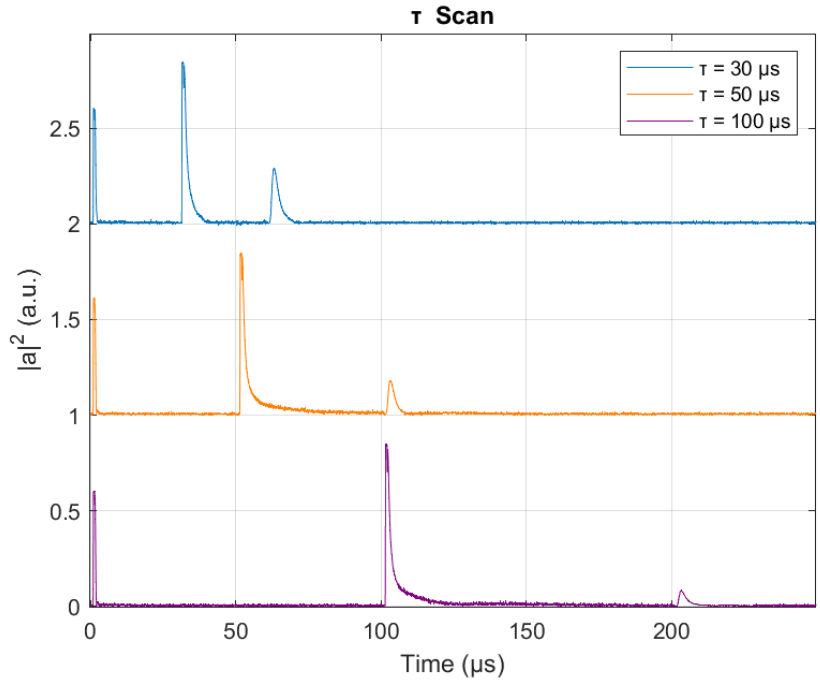

Figure 4.4: Measured traces for three different delay times τ, showing the characteristic formation of spin echoes. The three curves correspond to $\tau = 30\,\mu$s, $\tau = 50\,\mu$s, and $\tau = 100\,\mu$s, from top to bottom. The signals have been vertically offset for clarity. Each trace begins with two large signals caused by the applied $\pi/2$ and π pulses, separated by a delay τ, followed by a spin echo appearing at time 2τ after the initial $\pi/2$ pulse. The echo amplitude decreases with increasing delay time τ. The relative heights of the applied $\pi/2$ and π pulses appear slightly distorted due to saturation in the room-temperature amplifier of the output line.

In order to determine the optimal excitation conditions for our Hahn echo, a series of measurements at a fixed delay time τ was performed, systematically varying the amplitude and duration of the $\pi/2$ pulse. For each setting, the resulting echo signal was recorded and the echo peak heights were compared. The optimal parameters were identified as those producing the largest echo amplitude. Between consecutive measurements, we waited approximately 15 minutes, about 2 times the relaxation time T_1, to allow the spin ensemble to return to its initial ground state before repeating the Hahn echo sequence.

Finally, the coherence time T_2 was extracted by repeating the Hahn echo sequence at various delay times τ, ranging from $30\,\mu$s to 1 ms, at a temperature of 65 mK. Between each measurement, the system was allowed to relax for approximately 15 minutes, ensuring that the spin ensemble returned to its ground state before the next sequence. For each τ, the echo amplitude was recorded and plotted as a function of the delay time τ. The resulting decay curve is shown in figure 4.5, fitted using the exponential model introduced in section 2.2.2 (see also figure 2.11). The extracted coherence time is $T_2 = 768^{+64}_{-53}\,\mu$s, with uncertainties corresponding to a 90% confidence interval.

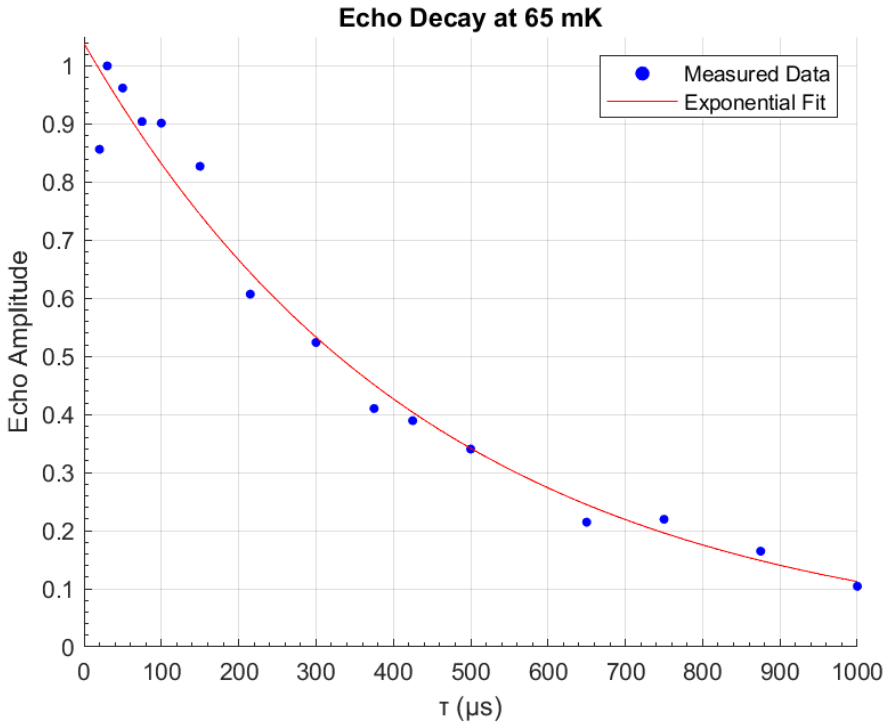

Figure 4.5: Decay of the Hahn echo amplitude as a function of the interpulse delay τ at 65 mK. Each point represents the measured echo amplitude after allowing full relaxation between runs. The solid line shows an exponential fit from which the coherence time T_2 is extracted.

To investigate the temperature dependence of coherence, the experiment was repeated at an elevated temperature of 150 mK. The same procedure was followed, including 15-minute relaxation intervals between each measurement. The corresponding decay curve and fit are shown in figure 4.6. The extracted coherence time at this higher temperature is $T_2 = 639^{+48}_{-34}\,\mu$s, indicating stronger dephasing compared to the 65 mK case. This reduction in coherence time can be attributed to increased interactions with the spin environment and the phonon bath at higher temperatures, which cause fluctuations in the local magnetic field experienced by the spins. These fluctuations lead to spectral diffusion, a process where the resonance frequencies of the spins drift over time, making phase refocusing less effective and thus shortening T_2 [52].

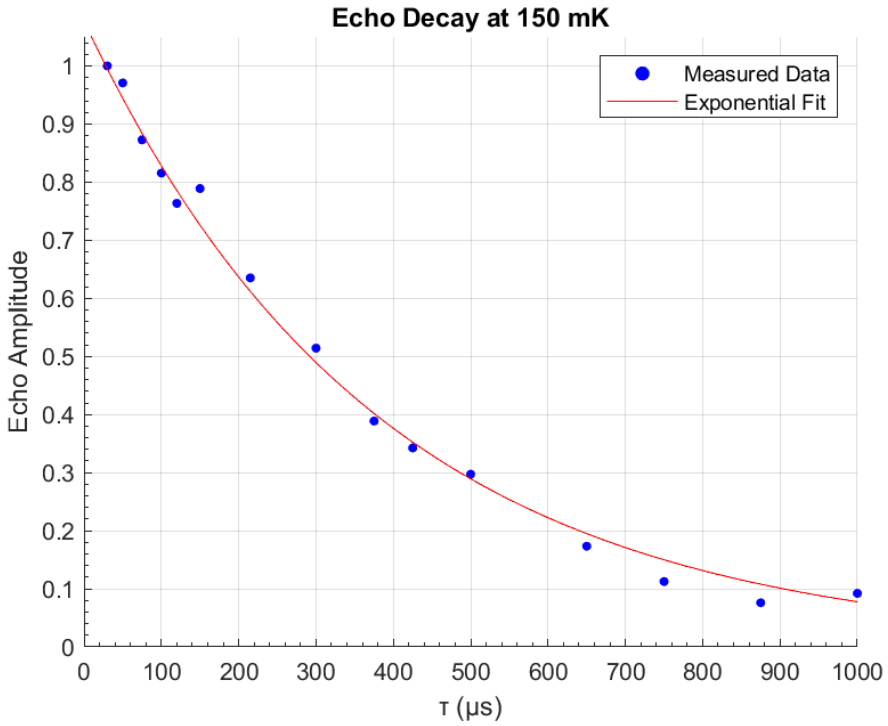

Figure 4.6: Hahn echo amplitude decay at 150 mK. As in the 65 mK case, the data is fitted with an exponential decay function. The extracted T_2 is shorter, indicating stronger spin dephasing at elevated temperatures.

4.2.2 Carr–Purcell–Meiboom–Gill

To further extend the coherence time of the sodium spin ensemble beyond the limitation set by inhomogeneous broadening, we employed the Carr–Purcell–Meiboom–Gill (CPMG) pulse sequence. This technique, introduced in section 2.2.3, counters spin dephasing by applying a series of equally spaced π pulses following an initial $\pi/2$ pulse.

In our experiment, rectangular pulses were used, generated by the same AWG setup as described in section 3.3. The CPMG sequence consisted of an initial $\pi/2$ pulse followed by a train of $N = 30$ refocusing π pulses, each separated by a delay $\tau = 100\,\mu$s. Following each π pulse, a spin echo was observed and recorded.

The data were averaged over 20 subsequent measurements to improve signal-to-noise ratio. Between each measurement, we again allowed the spin ensemble to relax for 15 minutes to ensure full thermalization and consistent initial conditions. The extracted echo peaks were then plotted as a function of total evolution time, and fitted using the exponential decay model introduced in section 2.2.3 to extract the coherence time T_2.

Figure 4.7 shows the results of the CPMG measurement at 115 mK. The blue curve is the averaged signal over 20 repetitions of the pulse sequence, revealing a series of

spin echoes following each refocusing π pulse. The echo peaks were extracted from this averaged trace and are shown as black dots. The first echo peak was excluded from the analysis, as it consistently exhibited anomalous behavior compared to the rest of the sequence. The remaining peaks were fitted using a single-exponential decay function, yielding a coherence time of $T_2 = 1.36^{+0.09}_{-0.06}$ ms. Compared to the Hahn echo results 4.2.1, the CPMG sequence extends the coherence time by almost a factor of two, demonstrating the effectiveness of dynamic decoupling in mitigating decoherence in our system.

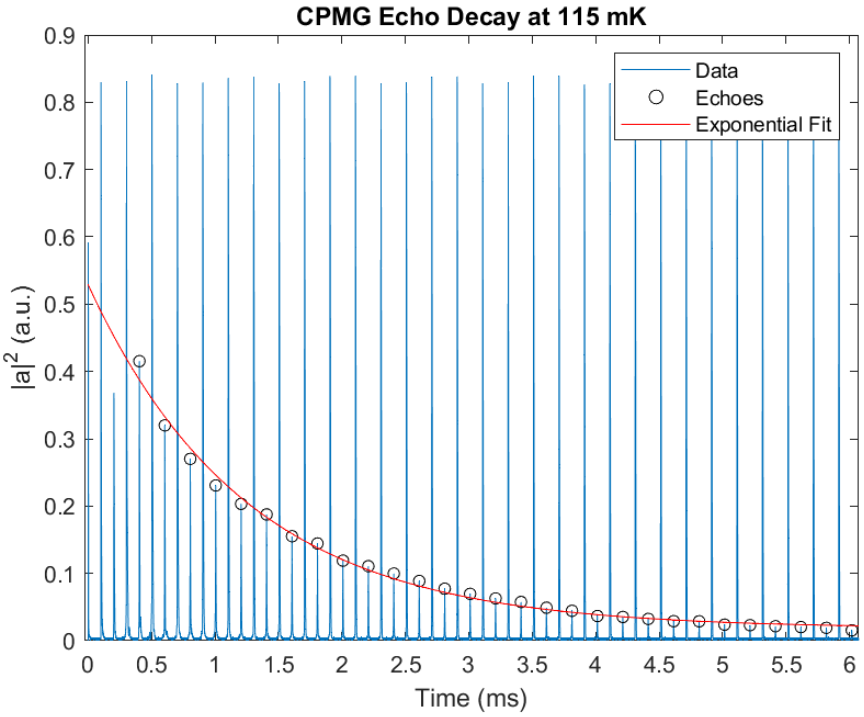

Figure 4.7: Averaged CPMG signal at 115 mK, showing a sequence of echoes following $N = 30$ refocusing pulses with $\tau = 100\,\mu$s. The blue curve represents the averaged signal, and the black dots mark the extracted echo peak amplitudes. These peaks are fitted with an exponential decay (red curve), yielding a coherence time of $T_2 = 1.36^{+0.09}_{-0.06}$ ms.

5 Conclusion and Outlook

In this work, we demonstrated strong coupling between a superconducting microwave resonator and a spin ensemble of sodium atoms embedded in a cryogenic solid neon matrix 4.1. Through a magnetic field scan, we observed vacuum Rabi splitting in the transmission spectrum, confirming that our hybrid quantum system operates in the strong coupling regime. The extracted cooperativity and the observation of polariton branches provided direct evidence of coherent coupling between collective spin excitations and the cavity mode.

We then turned to time-domain measurements to characterize the coherence properties of the spin ensemble. Hahn echo experiments 4.2.1 at 65 mK and 150 mK yielded coherence times of $T_2 = 768^{+64}_{-53}\,\mu$s and $T_2 = 639^{+48}_{-34}\,\mu$s, respectively, indicating that coherence is at least moderately temperature-dependent consistent with observations in other systems [52]. By applying a Carr–Purcell–Meiboom–Gill (CPMG) sequence 4.2.2 with $N = 30$ refocusing pulses, we extended the coherence time to $T_2 = 1.36^{+0.09}_{-0.06}$ ms, highlighting the effectiveness of dynamical decoupling in mitigating dephasing effects. Unlike the single Hahn echo pulse, the CPMG protocol repeatedly applies π pulses that refocus spin dephasing caused not only by inhomogeneous broadening but also by low-frequency noise and dipolar spin-spin interactions within the ensemble [33, 53, 54]. As also discussed in [55], increasing the number of refocusing pulses is essential for counteracting low-frequency noise.

The observed coherence times remain limited by inhomogeneous broadening and magnetic field fluctuations, which are prominent decoherence mechanisms in dense spin ensembles. Spectral diffusion and interactions between nearby spins are also expected to contribute, particularly at longer timescales. Notably, the coherence time obtained using the CPMG sequence is significantly longer than that extracted from the Hahn echo. This improvement arises because the CPMG protocol, with its multiple refocusing π pulses, dynamically suppresses low-frequency noise and inhomogeneous dephasing more effectively than the single-echo Hahn sequence. In our case, the use of $N = 30$ refocusing pulses extended T_2 by approximately a factor of two. Similar enhancements have been observed in other hybrid quantum systems employing dynamic decoupling techniques [56–58].

These results suggest that further improvements could be achieved by implement-

ing more advanced dynamical decoupling protocols, such as XY8 [53] or Uhrig [33] sequences, which provide better suppression of decoherence arising from pulse imperfections and environmental noise. Looking ahead, this hybrid architecture offers a promising platform for memory-type protocols, including write-read experiments that aim to store and retrieve spin excitations through carefully timed pulse sequences [59]. In such protocols, a series of weak excitation pulses prepare partial coherence in the ensemble, which is later probed by a stronger retrieval pulse to assess the stored information. Additionally, complementary techniques such as spectral hole-burning [60] could help characterize the inhomogeneous broadening profile and reveal slow dephasing processes. Together, these approaches may enable the development of spin-based memories suitable for integration into larger quantum information processing architectures.

In addition to the results presented above, an interesting feature consistently observed during our Hahn echo measurements was the appearance of echo trains. During the Hahn echo measurements (see 4.2.1), especially after careful calibration of the pulse parameters, we consistently observed the appearance of echo trains: multiple secondary echoes following the main echo signal, as shown in figure 5.1. These additional echoes occurred at regular intervals τ after the primary echo and were reproducible across different measurement runs. Previous theoretical work has shown that in inhomogeneously broadened spin ensembles, the first Hahn echo can itself act as a refocusing pulse, leading to self-stimulated secondary echoes [61]. This mechanism is thought to arise from a combination of imperfect pulse inversion and resonator-mediated collective back-action, which together result in constructive rephasing events and the formation of echo trains. Experimental confirmation of this effect has been reported in strongly coupled phosphorus donor spin ensembles [62], and similar observations have been made in other solid-state spin systems. The persistence of this effect in our Na:Ne system suggests it may be an intrinsic feature of inhomogeneously broadened ensembles with strong spin–photon coupling. However, its precise mechanism remains unknown. For the purpose of determining the coherence time T_2 in section 4.2.1, only the amplitude of the first (strongest) echo in the train was used for the fit. Ongoing work in our group aims to investigate this effect through measurements and simulations to better understand its nature.

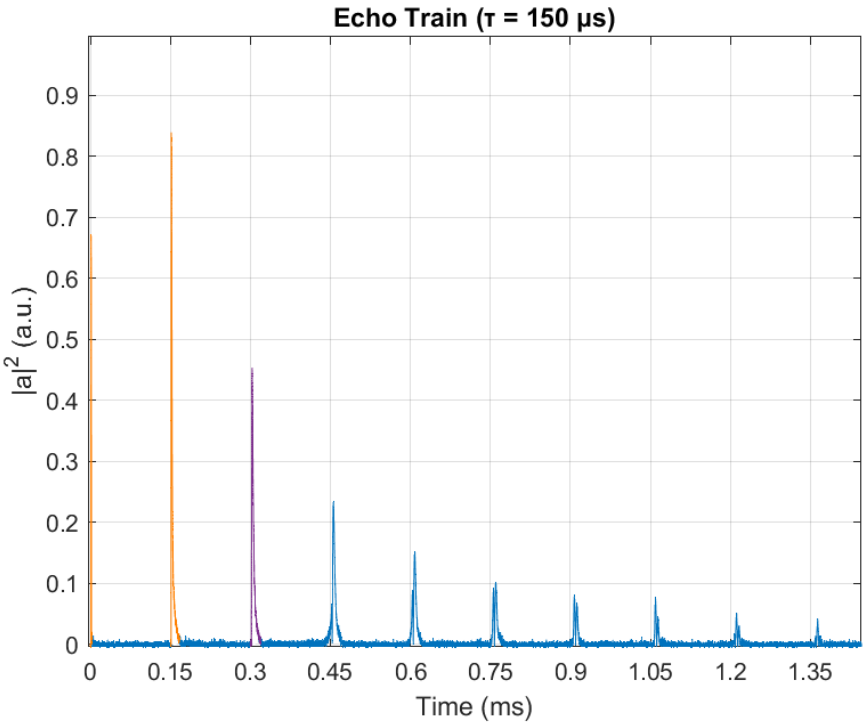

Figure 5.1: Hahn echo trace recorded in the Na:Ne spin ensemble, showing the $\pi/2$ and π pulses of the Hahn echo sequence (in orange) up to time $150\,\mu$s. The primary echo (in purple) appears at $300\,\mu$s, followed by a series of weaker secondary echoes at regular intervals of $\tau = 150\,\mu$s.

Bibliography

[1] James Clerk Maxwell. "VIII. A dynamical theory of the electromagnetic field". In: *Philosophical transactions of the Royal Society of London* 155 (1865), pp. 459–512.

[2] Albert Einstein. "Über einen die Erzeugung und Verwandlung des Lichtes betreffenden heuristischen Gesichtspunkt [AdP 17, 132 (1905)]". In: *Annalen der Physik* 517 (2005), pp. 164–181.

[3] The Nobel Prize Committee. *The Nobel Prize in Physics 1921*. `https://www.nobelprize.org/prizes/physics/1921/summary/`.

[4] Richard P. Feynman. *QED: The Strange Theory of Light and Matter*. Princeton, NJ: Princeton University Press, 1985.

[5] Serge Haroche and Jean-Michel Raimond. *Exploring the Quantum: Atoms, Cavities, and Photons*. Oxford University Press, 2006.

[6] Edward M. Purcell. "Spontaneous Emission Probabilities at Radio Frequencies". In: *Physical Review* 69 (1946), p. 681.

[7] Gershon Kurizki et al. "Quantum technologies with hybrid systems". In: *Proceedings of the National Academy of Sciences* 112.13 (2015), pp. 3866–3873.

[8] David I. Schuster et al. "High-Cooperativity Coupling of Electron-Spin Ensembles to Superconducting Cavities". In: *Physical Review Letters* 105.14 (2010), p. 140501.

[9] Robert H. Dicke. "Coherence in Spontaneous Radiation Processes". In: *Physical Review* 93 (1954), pp. 99–110.

[10] Andreas Angerer et al. "Superradiant emission from colour centres in diamond". In: *Nature Physics* 14.12 (2018), pp. 1168–1172.

[11] Wenzel Kersten et al. "Triggered superradiance and spin inversion storage in a hybrid quantum system". In: *Physical Review Letters* 131.4 (2023), p. 043601.

[12] Stefan Putz et al. "Protecting a spin ensemble against decoherence in the strong-coupling regime of cavity QED". In: *Nature Physics* 10 (2014), pp. 720–724.

[13] Dmitry O. Krimer et al. "Non-Markovian dynamics of a single-mode cavity strongly coupled to an inhomogeneously broadened spin ensemble". In: *Physical Review A* 90.4 (Oct. 2014), p. 043852.

[14] Marlan O. Scully and M. Suhail Zubairy. *Quantum Optics*. Cambridge University Press, 1997.

[15] Anthony Mark Fox. *Quantum optics: an introduction*. Vol. 15. Oxford university press, 2006.

[16] Christopher C Gerry and Peter L Knight. *Introductory quantum optics*. Cambridge university press, 2023.

[17] Claude Cohen-Tannoudji, Jacques Dupont-Roc, and Gilbert Grynberg. *Photons and atoms: introduction to quantum electrodynamics*. John Wiley & Sons, 2024.

[18] Edwin T Jaynes and Frederick W Cummings. "Comparison of quantum and semiclassical radiation theories with application to the beam maser". In: *Proceedings of the IEEE* 51.1 (1963), pp. 89–109.

[19] K. M. Birnbaum et al. "Photon blockade in an optical cavity with one trapped atom". In: *Nature* 436.7047 (2005), pp. 87–90. DOI: 10.1038/nature03804.

[20] Michael Tavis and Frederick W Cummings. "Exact solution for an N-molecule—radiation-field Hamiltonian". In: *Physical Review* 170.2 (1968), p. 379.

[21] Nikolaus De Zordo. "Using an inverted spin ensemble as a photon source". MA thesis. Technische Universität Wien, 2021.

[22] Howard J Carmichael. *Statistical methods in quantum optics 1: master equations and Fokker-Planck equations*. Springer Science & Business Media, 2013.

[23] Andreas Angerer. "Non-linear Dynamics in Cavity QED: Beyond Two Coupled Springs". PhD thesis. TU Wien, 2019.

[24] Constantino Tsallis. "Possible generalization of Boltzmann-Gibbs statistics". In: *Journal of statistical physics* 52.1 (1988), pp. 479–487.

[25] Brian Julsgaard and Klaus Mølmer. "Dynamical evolution of an inverted spin ensemble in a cavity: Inhomogeneous broadening as a stabilizing mechanism". In: *Physical Review A—Atomic, Molecular, and Optical Physics* 86.6 (2012), p. 063810.

[26] Michael A Nielsen and Isaac L Chuang. *Quantum Computation and Quantum Information*. Cambridge University Press, 2002.

[27] Charles P Slichter. *Principles of magnetic resonance*. Vol. 1. Springer Science & Business Media, 2013.

[28] Malcolm H Levitt. *Spin dynamics: basics of nuclear magnetic resonance*. John Wiley & Sons, 2008.

[29] Erwin L Hahn. "Spin echoes". In: *Physical review* 80.4 (1950), p. 580.

[30] Anatole Abragam. *The principles of nuclear magnetism*. 32. Oxford university press, 1961.

[31] James Keeler. *Understanding NMR spectroscopy*. John Wiley & Sons, 2011.

[32] Lorenza Viola and Seth Lloyd. "Dynamical suppression of decoherence in two-state quantum systems". In: *Physical Review A* 58.4 (1998), p. 2733.

[33] Götz S Uhrig. "Keeping a quantum bit alive by optimized π-pulse sequences". In: *Physical Review Letters* 98.10 (2007), p. 100504.

[34] Herman Y Carr and Edward M Purcell. "Effects of diffusion on free precession in nuclear magnetic resonance experiments". In: *Physical review* 94.3 (1954), p. 630.

[35] S Meiboom and D Gill. "Modified spin-echo method for measuring nuclear relaxation times". In: (1958).

[36] Kaveh Khodjasteh and Daniel A Lidar. "Fault-tolerant quantum dynamical decoupling". In: *Physical review letters* 95.18 (2005), p. 180501.

[37] Wen Yang, Zhen-Yu Wang, and Ren-Bao Liu. "Preserving qubit coherence by dynamical decoupling". In: *Frontiers of Physics in China* 6.1 (2011), pp. 2–14.

[38] Daniel A. Steck. *Sodium D Line Data*. `http://steck.us/alkalidata`. Revision 2.3.3, 28 May 2024. 2024.

[39] Pieter Zeeman. "The effect of magnetisation on the nature of light emitted by a substance". In: *nature* 55.1424 (1897), p. 347.

[40] Brian Harold Bransden and Charles Jean Joachain. *Physics of atoms and molecules*. Pearson Education India, 2003.

[41] Stefan Weichselbaumer et al. "Quantitative Modeling of Superconducting Planar Resonators for Electron Spin Resonance". In: *Phys. Rev. Appl.* 12 (2 Aug. 2019), p. 024021.

[42] Ugo Fano. "Effects of configuration interaction on intensities and phase shifts". In: *Physical review* 124.6 (1961), p. 1866.

[43] Andrey E Miroshnichenko, Sergej Flach, and Yuri S Kivshar. "Fano resonances in nanoscale structures". In: *Reviews of Modern Physics* 82.3 (2010), pp. 2257–2298.

[44] STAR Cryoelectronics. *Cryostats*. `https://starcryo.com/adr-cryostats/`. 2024.

[45] Andrew N. Kanagin. "Design and Modeling of a Cryogenic System for Circuit QED Experiments". Master's thesis. Reno, NV: University of Nevada, Reno, 2018.

[46] Andrew N. Kanagin. "Coupling in Quantum Solids: From Atoms Towards Molecules". PhD thesis. Technische Universität Wien, 2025.

[47] Takayuki Iwasaki et al. "Tin-vacancy quantum emitters in diamond". In: *Physical review letters* 119.25 (2017), p. 253601.

[48] Zhenrong Zhang et al. "Investigation of zero-phonon line characteristics in ensemble nitrogen-vacancy centers at 1.6 K–300 K". In: *Optics Express* 32.10 (2024), pp. 17336–17344.

[49] W. N. Kersten. "A masing diamond: Triggered and self-induced superradiance". Dissertation. Technische Universität Wien, 2025.

[50] Ludwig Boltzmann. "Uber die Beziehung zwischen dem zweiten Hauptzatze der mechanischen Warmetheorie und der Wahrscheinlichkeitsrechnung, respective den Satzen uber das Warmegleichgewicht". In: (1877).

[51] Raj Kumar Pathria. *Statistical Mechanics: International Series of Monographs in Natural Philosophy*. Vol. 45. Elsevier, 2017.

[52] Alexei M Tyryshkin et al. "Electron spin coherence exceeding seconds in high-purity silicon". In: *Nature materials* 11.2 (2012), pp. 143–147.

[53] Terry Gullion, David B Baker, and Mark S Conradi. "New, compensated Carr-Purcell sequences". In: *Journal of Magnetic Resonance (1969)* 89.3 (1990), pp. 479–484.

[54] Gijs De Lange et al. "Universal dynamical decoupling of a single solid-state spin from a spin bath". In: *Science* 330.6000 (2010), pp. 60–63.

[55] Ioannis Karapatzakis et al. "Microwave control of the tin-vacancy spin qubit in diamond with a superconducting waveguide". In: *Physical Review X* 14.3 (2024), p. 031036.

[56] Boris Naydenov et al. "Dynamical decoupling of a single-electron spin at room temperature". In: *Physical Review B—Condensed Matter and Materials Physics* 83.8 (2011), p. 081201.

[57] Linh My Pham et al. "Enhanced solid-state multispin metrology using dynamical decoupling". In: *Physical Review B—Condensed Matter and Materials Physics* 86.4 (2012), p. 045214.

[58] Sunil Upadhyay et al. "Ultralong spin-coherence times for rubidium atoms in solid parahydrogen via dynamical decoupling". In: *Physical Review Letters* 125.4 (2020), p. 043601.

[59] C Grezes et al. "Multimode storage and retrieval of microwave fields in a spin ensemble". In: *Physical Review X* 4.2 (2014), p. 021049.

[60] Stefan Putz et al. “Spectral hole burning and its application in microwave photonics”. In: *Nature Photonics* 11.1 (2017), pp. 36–39.

[61] Kamanasish Debnath et al. “Self-stimulated pulse echo trains from inhomogeneously broadened spin ensembles”. In: *Physical Review Letters* 125.13 (2020), p. 137702.

[62] Stefan Weichselbaumer et al. “Echo trains in pulsed electron spin resonance of a strongly coupled spin ensemble”. In: *Physical Review Letters* 125.13 (2020), p. 137701.

A Appendix

A.1 Derivation of the Transformed Hamiltonian

We start with equation (2.27) in the main text:

$$\hat{H}'(\vec{r},t) = \hat{U}^\dagger \hat{H}(\vec{r},t)\hat{U} - i\hbar\hat{U}^\dagger \frac{\partial \hat{U}}{\partial t} \tag{A1}$$

where the original Hamiltonian (2.22) is given by

$$\hat{H}(\vec{r},t) = \frac{1}{2m}[\hat{p} + e\vec{\mathbf{A}}(\vec{r},t)]^2 + V(\vec{r}) \tag{A2}$$

and the unitary transformation (2.28) is

$$\hat{U} = e^{i\chi(\vec{r},t)} \tag{A3}$$

First we notice that if an operator acts as multiplication in the position basis, it commutes with $\hat{U}$ because $\hat{U}$ is also multiplicative in $\vec{r}$. Therefore:

$$\begin{aligned} \hat{U}^\dagger \vec{A}(\vec{r},t)\hat{U} &= \vec{A}(\vec{r},t) \\ \hat{U}^\dagger V(\vec{r})\hat{U} &= V(\vec{r}) \end{aligned} \tag{A4}$$

Thus, the vector potential and the static potential remain unchanged under this part of the transformation. However, the canonical momentum $\hat{p} = -i\hbar\vec{\nabla}$ does not commute with $\hat{U}$. Acting on a wavefunction $\psi(\vec{r})$, we have:

$$\begin{aligned} \hat{U}^\dagger \hat{p}\hat{U}\psi(\vec{r}) &= e^{-i\chi(\vec{r},t)}\big[-i\hbar\vec{\nabla}\big(e^{i\chi(\vec{r},t)}\psi(\vec{r})\big)\big] \\ &= e^{-i\chi}\big[-i\hbar\big(i(\vec{\nabla}\chi)e^{i\chi}\psi(\vec{r}) + e^{i\chi}\vec{\nabla}\psi(\vec{r})\big)\big] \\ &= \big[\hat{\vec{p}} + \hbar\vec{\nabla}\chi(\vec{r},t)\big]\psi(\vec{r}) \end{aligned} \tag{A5}$$

Hence:

$$\hat{U}^\dagger \hat{p}\hat{U} = \hat{p} + \hbar\vec{\nabla}\chi(\vec{r},t) \tag{A6}$$

Thus, for the kinetic term in equation (A1) we get:

$$\hat{U}^\dagger \big[\hat{p} + e\,\vec{A}(\vec{r},t)\big]\hat{U} = \hat{p} + \hbar\vec{\nabla}\chi(\vec{r},t) + e\,\vec{A}(\vec{r},t) \tag{A7}$$

Squaring this:

$$\begin{aligned}\hat{U}^\dagger \big[\hat{p} + e\,\vec{A}(\vec{r},t)\big]^2\hat{U} &= \hat{U}^\dagger \big[\hat{p} + e\,\vec{A}(\vec{r},t)\big]\hat{U}\hat{U}^\dagger \big[\hat{p} + e\,\vec{A}(\vec{r},t)\big]\hat{U} \\ &= \big[\hat{p} + \hbar\vec{\nabla}\chi(\vec{r},t) + e\,\vec{A}(\vec{r},t)\big]^2\end{aligned} \tag{A8}$$

Putting it all together in equation (A1) and also computing the last term we get equation (2.29) in the main text:

$$\begin{aligned}\hat{H}'(\vec{r},t) = \hat{U}^\dagger\hat{H}(\vec{r},t)\hat{U} - i\hbar\hat{U}^\dagger\frac{\partial\hat{U}}{\partial t} = \\ = \frac{1}{2m}[\hat{p} + \hbar\vec{\nabla}\chi(\vec{r},t) + e\vec{\mathbf{A}}(\vec{r},t)]^2 + V(\vec{r}) + \hbar\frac{\partial\chi(\vec{r},t)}{\partial t}\end{aligned} \tag{A9}$$

A.2 Eigenvalues and Eigenvectors of the Jaynes-Cummings Hamiltonian

Starting from the Jaynes-Cummings Hamiltonian 2.44

$$\hat{H}_{JC} = \hbar\omega\hat{a}^\dagger\hat{a} + \frac{1}{2}\hbar\omega_a\hat{\sigma}_z + \hbar g\left(\hat{\sigma}_+\hat{a} + \hat{\sigma}_-\hat{a}^\dagger\right) \tag{A10}$$

we can write it in matrix form in the basis $|e,n\rangle, |g,n+1\rangle$ as:

$$\hat{H}_{JC} = \hbar\begin{pmatrix}\omega n + \frac{\omega_a}{2} & g\sqrt{n+1} \\ g\sqrt{n+1} & \omega(n+1) - \frac{\omega_a}{2}\end{pmatrix} \tag{A11}$$

The eigenvalues of this 2×2 matrix are found by solving: $\det\left(\hat{H}_{JC} - \lambda\mathbb{I}\right) = 0$:

$$\begin{aligned}&\left(\hbar\omega n + \frac{\hbar\omega_a}{2} - \lambda\right)\left(\hbar\omega(n+1) - \frac{\hbar\omega_a}{2} - \lambda\right) - \hbar^2 g^2(n+1) = 0 \\ \implies\ &\lambda^2 - \lambda\hbar\omega(2n+1) + \hbar^2\omega^2 n(n+1) + \frac{\hbar^2\omega\omega_a}{2} - \frac{\hbar^2\omega_a^2}{4} - \hbar^2 g^2(n+1) = 0\end{aligned} \tag{A12}$$

Solving this quadratic equation for λ gives the eigenvalues (2.45):

$$\lambda_{\pm} = \hbar\omega\left(n + \frac{1}{2}\right) \pm \frac{\hbar}{2}\Omega_n(\Delta) \tag{A13}$$

with $\Omega_n(\Delta) = \sqrt{4g^2\,(n+1) + \Delta^2}$ and the detuning $\Delta = \omega - \omega_a$.

We can now find the corresponding eigenvectors (dressed states) by starting from the 2×2 eigenvalue problem:

$$\hbar \begin{pmatrix} \omega n + \frac{\omega_a}{2} & g\sqrt{n+1} \\ g\sqrt{n+1} & \omega(n+1) - \frac{\omega_a}{2} \end{pmatrix} \begin{pmatrix} c_e \\ c_g \end{pmatrix} = \lambda \begin{pmatrix} c_e \\ c_g \end{pmatrix} \tag{A14}$$

The components c_e, c_g satisfy:

$$\begin{aligned} \big(\hbar\omega n + \tfrac{\hbar\omega_a}{2} - \lambda\big)c_e + \hbar g\sqrt{n+1}\, c_g = 0 \\ \hbar g\sqrt{n+1}\, c_e + \big(\hbar\omega(n+1) - \tfrac{\hbar\omega_a}{2} - \lambda\big)c_g = 0 \end{aligned} \tag{A15}$$

From the first line in (A15) and by substituting the eigenvalues (A13) we have:

$$\frac{c_g}{c_e} = -\frac{\omega n + \frac{\omega_a}{2} - \lambda/\hbar}{g\sqrt{n+1}} = \frac{\Delta \pm \Omega_n(\Delta)}{2g\sqrt{n+1}} \tag{A16}$$

We define the angle θ_n by

$$\theta_n = \tan^{-1}\left(\frac{2g\sqrt{n+1}}{\Delta}\right) \tag{A17}$$

with

$$\cos\theta_n = \frac{\Delta}{\Omega_n(\Delta)}, \quad \sin\theta_n = \frac{2g\sqrt{n+1}}{\Omega_n(\Delta)}$$

Using the half-angle trigonometric identity, we obtain:

$$\tan\left(\frac{\theta_n}{2}\right) = \frac{\sin\theta_n}{1+\cos\theta_n} = \frac{2g\sqrt{n+1}}{\Omega_n(\Delta) + \Delta} \tag{A18}$$

One can easily check the following relations:

$$\cot\left(\frac{\theta_n}{2}\right) = \frac{\Omega_n(\Delta) + \Delta}{2g\sqrt{n+1}}, \quad \tan\left(\frac{\theta_n}{2}\right) = \frac{\Omega_n(\Delta) - \Delta}{2g\sqrt{n+1}} \tag{A19}$$

Comparing (A19) to the ratios in equation (A16) one can see that

$$\frac{c_g}{c_e}\Big|_+ = \cot\left(\frac{\theta_n}{2}\right), \quad \frac{c_g}{c_e}\Big|_- = -\tan\left(\frac{\theta_n}{2}\right) \tag{A20}$$

such that one gets the eigenvectors (2.46):

$$\begin{aligned} |n,+\rangle &= \sin\left(\frac{\theta_n}{2}\right)|e,n\rangle + \cos\left(\frac{\theta_n}{2}\right)|g,n+1\rangle \\ |n,-\rangle &= \cos\left(\frac{\theta_n}{2}\right)|e,n\rangle - \sin\left(\frac{\theta_n}{2}\right)|g,n+1\rangle \end{aligned} \tag{A21}$$

A.3 Eigenvalues of the Energy-Shifted Jaynes-Cummings Hamiltonian

We start from the shifted Jaynes-Cummings Hamiltonian (2.50)

$$\hat{H}_{JC} = \hbar\omega\hat{a}^\dagger\hat{a} + \hbar\omega_a\hat{\sigma}_+\hat{\sigma}_- + \hbar g\left(\hat{\sigma}_+\hat{a} + \hat{\sigma}_-\hat{a}^\dagger\right) \tag{A22}$$

and write it again in matrix form in the basis $\{|e,n\rangle, |g,n+1\rangle\}$ as:

$$\hat{H}_{JC} = \hbar\begin{pmatrix} \omega n + \omega_a & g\sqrt{n+1} \\ g\sqrt{n+1} & \omega(n+1) \end{pmatrix} \tag{A23}$$

The eigenvalues are obtained again by solving the characteristic equation:

$$\det\left(\hat{H}_{JC} - \lambda\mathbb{I}\right) = 0 \implies (\hbar\omega n + \hbar\omega_a - \lambda)\left(\hbar\omega(n+1) - \lambda\right) - \hbar^2 g^2(n+1) = 0 \tag{A24}$$

Solving this quadratic equation for λ gives (2.51):

$$\lambda_\pm = \hbar\omega\left(n + \frac{1}{2}\right) + \frac{1}{2}\hbar\omega_a \pm \frac{\hbar}{2}\Omega_n(\Delta) \tag{A25}$$

with $\Omega_n(\Delta) = \sqrt{4g^2(n+1) + \Delta^2}$ and the detuning $\Delta = \omega - \omega_a$.

A.4 Interaction Picture Jaynes-Cummings Hamiltonian

Starting from the shifted Jaynes-Cummings Hamiltonian in the Schrödinger picture (2.50):

$$\hat{H}_{JC} = \hat{H}_0 + \hat{H}_{\text{int}}, \quad \hat{H}_0 = \hbar\omega\hat{a}^\dagger\hat{a} + \hbar\omega_a\hat{\sigma}_+\hat{\sigma}_-, \quad \hat{H}_{\text{int}} = \hbar g\left(\hat{\sigma}_+\hat{a} + \hat{\sigma}_-\hat{a}^\dagger\right) \tag{A26}$$

the interaction picture Hamiltonian is defined as (2.52):

$$\hat{H}_{\text{int}}(t) = e^{\frac{i}{\hbar}\hat{H}_0 t}\hat{H}_{\text{int}}e^{\frac{-i}{\hbar}\hat{H}_0 t} \tag{A27}$$

For the field operators, we can apply the Baker–Campbell–Hausdorff formula [14]

$$e^{\lambda\hat{A}}\,\hat{B}\,e^{-\lambda\hat{A}} = \hat{B} + \lambda[\hat{A},\hat{B}] + \frac{\lambda^2}{2!}[\hat{A},[\hat{A},\hat{B}]] + \frac{\lambda^3}{3!}[\hat{A},[\hat{A},[\hat{A},\hat{B}]]] + \dots \tag{A28}$$

and use the commutator $[\hat{a}^\dagger\hat{a},\hat{a}] = -\hat{a}$, which gives

$$\hat{a}(t) = \hat{a}\,e^{-i\omega t}, \quad \hat{a}^\dagger(t) = \hat{a}^\dagger\,e^{i\omega t} \tag{A29}$$

Similarly, for the atomic raising and lowering operators, using $[\hat{\sigma}_+\hat{\sigma}_-,\hat{\sigma}_+] = \hat{\sigma}_+$ and $[\hat{\sigma}_+\hat{\sigma}_-,\hat{\sigma}_-] = -\hat{\sigma}_-$, we obtain

$$\hat{\sigma}_+(t) = \hat{\sigma}_+\,e^{i\omega_a t}, \quad \hat{\sigma}_-(t) = \hat{\sigma}_-\,e^{-i\omega_a t} \tag{A30}$$

Substituting these results into equation (A27), we find (2.53)

$$\begin{aligned}\hat{H}_{\text{int}}(t) &= \hbar g\left[\hat{\sigma}_+(t)\hat{a}(t) + \hat{\sigma}_-(t)\hat{a}^\dagger(t)\right] \\ &= \hbar g\left[\hat{\sigma}_+\hat{a}e^{-i(\omega-\omega_a)t} + \hat{\sigma}_-\hat{a}^\dagger e^{i(\omega-\omega_a)t}\right] \\ &= \hbar g\left(\hat{\sigma}_+\hat{a}e^{-i\Delta t} + \hat{\sigma}_-\hat{a}^\dagger e^{i\Delta t}\right)\end{aligned} \tag{A31}$$